The Astrophysical Journal, 745:181 (22pp), 2012 February 1 doi:10.1088/0004-637X/745/2/181

AKARI OBSERVATION OF THE NORTH ECLIPTIC POLE (NEP) SUPERCLUSTER AT $z = 0.087$: MID-INFRARED VIEW OF TRANSITION GALAXIES

Jongwan Ko[1,2,3,4], Myungshin Im[3,4], Hyung Mok Lee[3], Myung Gyoon Lee[3], Seong Jin Kim[3], Hyunjin Shim[5], Yiseul Jeon[3,4], Ho Seong Hwang[6], Christopher N. A. Willmer[7], Matthew A. Malkan[8], Casey Papovich[9], Benjamin J. Weiner[7], Hideo Matsuhara[10], Shinki Oyabu[11], and Toshinobu Takagi[10]
[1] Yonsei University Observatory, Yonsei University, Seoul 120-749, Republic of Korea; jwko@yonsei.ac.kr
[2] Korea Astronomy and Space Science Institute, Daejeon 305-348, Republic of Korea
[3] Astronomy Program, Department of Physics & Astronomy, FPRD, Seoul National University, Seoul 151-742, Republic of Korea
[4] Center of the Exploration of the Origin of the Universe (CEOU), Seoul National University, Seoul, Republic of Korea
[5] Spitzer Science Center, California Institute of Technology, MS 220-6, Pasadena, CA 91125, USA
[6] Service d'Astrophysique, CEA Saclay, F-91191 Gif-sur-Yvette, France
[7] Steward Observatory, University of Arizona, 933 North Cherry Avenue, Tucson, AZ 85721, USA
[8] Department of Physics and Astronomy, University of California at Los Angeles, CA 90095, USA
[9] George P. and Cynthia W. Mitchell Institute for Fundamental Physics and Astronomy, Department of Physics, Texas A&M University, College Station, TX 77843, USA
[10] Institute of Space and Astronautical Science, Japan Aerospace Exploration Agency, Kanagawa 229-8510, Japan
[11] Graduate School of Science, Nagoya University, Furo-cho, Chikusa-ku, Nagoya, Aichi 464-8602, Japan
Received 2011 September 9; accepted 2011 November 28; published 2012 January 17

ABSTRACT

We present the mid-infrared (MIR) properties of galaxies within a supercluster in the north ecliptic pole region at $z \sim 0.087$ observed with the *AKARI* satellite. We use data from the *AKARI* NEP-Wide (5.4 deg^2) IR survey and the CLusters of galaxies EVoLution studies (CLEVL) mission program. We show that near-IR (3 μm)–mid-IR (11 μm) color can be used as an indicator of the specific star formation rate and the presence of intermediate-age stellar populations. From the MIR observations, we find that red-sequence galaxies consist not only of passively evolving red early-type galaxies, but also of (1) "weak-SFGs" (disk-dominated star-forming galaxies that have star formation rates lower by $\sim$4 $\times$ than blue-cloud galaxies) and (2) "intermediate-MXGs" (bulge-dominated galaxies showing stronger MIR dust emission than normal red early-type galaxies). These two populations can be a set of transition galaxies from blue, star-forming, late-type galaxies evolving into red, quiescent, early-type ones. We find that the weak-SFGs are predominant at intermediate masses ($10^{10}\,M_\odot < M_* < 10^{10.5}\,M_\odot$) and are typically found in local densities similar to the outskirts of galaxy clusters. As much as 40% of the supercluster member galaxies in this mass range can be classified as weak-SFGs, but their proportion decreases to <10% at larger masses ($M_* > 10^{10.5}\,M_\odot$) at any galaxy density. The fraction of the intermediate-MXG among red-sequence galaxies at $10^{10}\,M_\odot < M_* < 10^{11}\,M_\odot$ also decreases as the density and mass increase. In particular, $\sim$42% of the red-sequence galaxies with early-type morphologies are classified as intermediate-MXGs at intermediate densities. These results suggest that the star formation activity is strongly dependent on the stellar mass, but that the morphological transformation is mainly controlled by the environment.

Key words: galaxies: clusters: general – galaxies: evolution – galaxies: stellar content – infrared: galaxies – surveys

Online-only material: color figures

1. INTRODUCTION

One of the leading factors that can strongly influence galaxy evolution is the environment. Observationally, it has been known that the environment plays an important role in shaping galaxy properties (see Blanton & Moustakas 2009 for a review). The morphology–density relation (MDR) was first described by Dressler (1980), who found a strong correlation between the morphological type fraction and local galaxy surface density, where, for increasing local density, the fraction of elliptical galaxies increases, while the spiral fraction decreases. Since then, a number of studies have reported that galaxy properties, such as colors and star formation activity (SFA), are also strongly dependent on the local density (e.g., Park & Hwang 2009). MDR was also found at $z \sim 1$ (e.g., Postman et al. 2005; Hwang & Park 2009). Similarly, the fraction of blue, star-forming (SF) galaxies decreases as the density increases, which is known as the color–density relation (CDR; e.g., Lewis et al. 2002; Balogh et al. 2004; Koopmann & Kenney 2004). More recently, using the galaxies in the Galaxy Zoo project (Lintott et al. 2008), Bamford et al. (2009) studied the dependence of galaxy color and morphology on environment, and showed that galaxy color has a much stronger dependency on environment than morphology at fixed stellar mass. This is consistent with the result of Blanton et al. (2005), which suggests that the color seems to be very sensitive to the local density.

Besides environment, there is also a clear tendency for massive galaxies at low redshift to be red, quiescent, and have early-type morphologies, indicating that the galaxy properties also correlate with stellar mass. Kauffmann et al. (2003), using the Sloan Digital Sky Survey (SDSS; York et al. 2000) data, showed that low-redshift galaxies divide into two distinct populations at a stellar mass of $3 \times 10^{10}\,M_\odot$: lower-mass galaxies have young stellar populations and low-concentration indices typical of disk systems. Baldry et al. (2006) also found that the color–mass relations do not depend strongly on

environment, while the fraction of red galaxies depends both on mass and environment. They also found that models with internally driven feedback mechanisms can explain the observed properties better. In a different study, Bundy et al. (2006) investigated the mass-dependent evolution of galaxies for $0.4 < z < 1.4$, and found that there is no significant correlation between environment and the "downsizing" trend—in which massive galaxies are older because their SFA finished earlier (Cowie et al. 1996). This suggests that quenching of star formation in massive galaxies is primarily internally driven. This idea is also consistent with recent findings using $z \sim 1$ samples, that the SFA is most strongly driven by stellar mass (e.g., Peng et al. 2010; Li et al. 2011; Sobral et al. 2011).

Therefore, the question of whether mass or environment is a main driving factor for changes in color and morphology, and how they have affected the evolution of galaxies remain one of the controversial issues of galaxy evolution. We cannot track individual galaxies as they evolve with time from their birth. In the local universe, we can only see evolutionary snapshot pictures of galaxies from which we infer their evolution indirectly. Galaxies in the transition phase from blue to red and from spiral to spheroidal are particularly useful targets to study the evolutionary mechanisms. In this paper, we focus on these transition populations, and explore their dependence on mass and environment.

Clusters and superclusters are excellent astrophysical laboratories of galaxy evolution. These structures provide a wide range of environments, ranging from low density at the outskirts to the high-density regions at the cluster centers. They also contain a wide range of galaxy masses—from low-mass dwarf galaxies ($M_* \sim 10^7\ M_\odot$) to the most massive galaxies ($M_* \sim 10^{13}\ M_\odot$). In addition to the MDR and the CDR mentioned earlier, the number of SF galaxies (blue galaxies) in clusters increases toward higher redshift (the Butcher–Oemler effect; Butcher & Oemler 1984), and the number of S0 galaxies seems to decline rapidly with redshift, with a corresponding increase in the blue, spiral galaxies (e.g., Dressler et al. 1997; Poggianti et al. 2001). At higher redshift, the star formation rates (SFRs) in high-density environments seem to be steadily increasing (Elbaz et al. 2007). These observational findings led to suggestions of physical mechanisms to transform blue spirals into red spheroids. The suggested mechanisms are either gravitational (e.g., tidal interaction) or hydrodynamic (e.g., ram-pressure stripping or removal of the gas supply and quenching of star formation by halo; see Boselli & Gavazzi 2006 and Park & Hwang 2009).

Many researchers have used optical colors or spectral features as a proxy of SFA to study the galaxy properties in cluster environments. Stellar masses of galaxies are usually obtained by fitting the spectral energy distributions (SEDs) measured by UV and optical photometry. Large data sets of galaxies, such as the SDSS, have been used to understand the galaxy evolution in cluster environments (e.g., Blanton & Moustakas 2009; Park & Hwang 2009). However, an obvious disadvantage of this approach using the UV/optical light is dust obscuration. The interstellar medium in galaxies has dust that absorbs the UV light from stars (mostly coming from young, hot stars). This leads to significant extinction of the UV and optical light, complicating the interpretation of the SFA. Fortunately, the absorbed UV/optical light is re-emitted in the infrared where one can obtain an unobscured view of the SFA. Earlier studies of the SFA in clusters were made with *Infrared Space Observatory* (e.g., Boselli et al. 1998; Biviano et al. 2004). More recently, *Spitzer* has revealed the SFA in clusters in the IR, finding a few clusters with exceptionally high SFRs, and the rapid evolution of the SFA as a function of redshift (Bai et al. 2009). Nevertheless, the study of the SFA in clusters, as a function of environment, has been limited.

In cluster environments, early-type galaxies follow a tight color–magnitude relation (CMR; red-sequence), indicating their stellar population is homogeneously old and passively evolving (e.g., Bower et al. 1992; Kodama & Arimoto 1997). However, early-type galaxies do not contain homogeneous stellar populations when we examine them at different wavelengths, particularly in the IR. Previous IR observations showed that there are some early-type galaxies with excess far-IR (FIR) emission (Knapp et al. 1989) and mid-IR (MIR) emission (Knapp et al. 1992; Xilouris et al. 2004). Recently, Clemens et al. (2009), using *Spitzer*-IRS peak-up images (16 μm), found that about 32% of the early-type galaxies in the Coma cluster have excess flux over photospheric emission in the MIR. Bressan et al. (2006) also detected MIR emission in early-type galaxies with *Spitzer*, showing a wide emission feature around 10 μm and another broad feature near 18 μm. Unusual polycyclic aromatic hydrocarbons (PAHs) are also detected in the NIR/MIR spectra of nearby early-type galaxies (Kaneda et al. 2005, 2008; Lee et al. 2010; Vega et al. 2010; Panuzzo et al. 2011). This suggests that they are associated with intermediate-age stellar populations, formed in a post-starburst phase.

The IR emission from early-type galaxies is attributed either to the Rayleigh–Jeans tail of the stellar photosphere or to circumstellar dust around evolved stars in the asymptotic giant branch (AGB). Theoretical works show that the MIR-excess emission of AGB stars is well correlated with stellar age (Piovan et al. 2003), and several studies suggest that MIR excess is a good age indicator (Temi et al. 2005; Ko et al. 2009; Shim et al. 2011). Indeed, the MIR-excess emission can be useful in tracing the past SFA, because other mean stellar age indicators cannot discriminate the emission of these stars.

In summary, earlier studies find that IR data are useful and perhaps critical in some cases to (1) obtain an unobscured view of the SFA and (2) trace recent SFA in early-type or red galaxies. However, the previous studies of IR properties of cluster galaxies have been mostly limited to the derivation of global properties of clusters or examining a limited number of individual galaxies. In addition, there are few studies focusing on the galaxy environment on much larger scales (such as across a supercluster). Therefore, it is necessary to study the effects of environment and/or mass on the IR properties of galaxies in clusters and superclusters.

Batuski & Burns (1985) first discovered the large-scale structure in the north ecliptic pole (NEP) region as an association of six clusters of galaxies, using a percolation analysis of clusters in Abell's (1958) catalog. Subsequently, Burg et al. (1992), using early observations with the *ROSAT* satellite, reported five X-ray clusters and groups at $0.08 < z < 0.09$ within $1\overset{\circ}{.}5$ of the NEP. With the deepest exposure of the *ROSAT* All-Sky Survey, Mullis et al. (2001) found an extended large-scale structure in the NEP region at $0.07 < z < 0.1$—the NEP supercluster—which consists of eight Abell clusters (A2255, A2295, A2301, A2304, A2308, A2311, A2312, and A2315). These X-ray detected clusters have luminosities in the range of $(0.2\text{–}3.6) \times 10^{44}\ h_{50}^{-2}$ erg s^{-1} (0.5–2.0 keV). In addition, they found three new clusters in this X-ray luminosity range, which are not contained in the optical cluster catalog, and ten groups

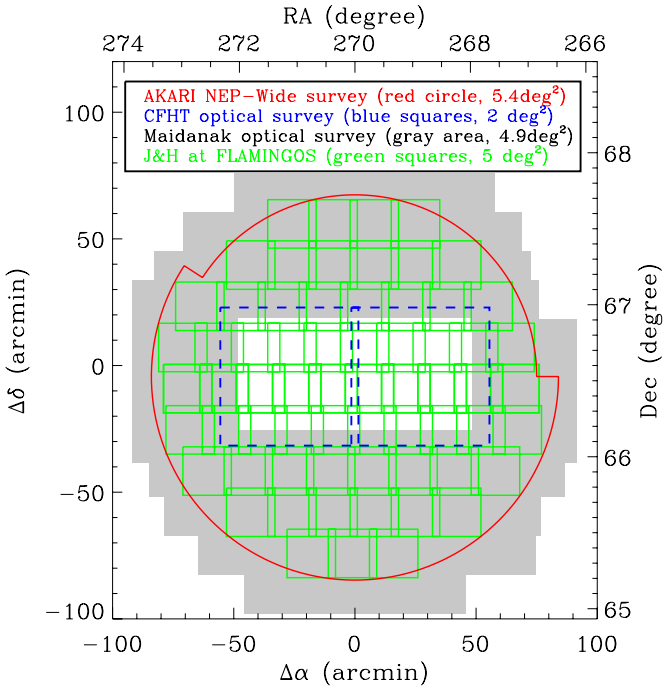

Figure 1. Imaging coverage of the ANWS. The center coordinates of the ANWS are at ($\alpha = 18^{h}00^{m}00^{s}$, $\delta = +66°36'00''$). North is up and east is to the left. The *AKARI* IR (2–24 μm) data (5.4 deg^2), CFHT Megacam $u^*g'r'i'z'$ data (2 deg^2), Maidanak *BRI* data (4.9 deg^2), and KPNO *JH* data (5 deg^2) are represented by the red solid circle, blue dashed squares, the gray shaded region, and green squares, respectively.

(A color version of this figure is available in the online journal.)

of galaxies with X-ray luminosities in the range of (2–9) $\times$ 10^{42} h_{50}^{-2} erg s^{-1} (0.5–2.0 keV).

Thanks to the *AKARI* IR Space Telescope (Murakami et al. 2007) and its Sun-synchronous orbit, we carried out an IR survey in the NEP region (5.4 deg^2) as part of the *AKARI* NEP-Wide survey (ANWS; see Figures 1 and 3). The main advantage of *AKARI* against previous IR satellites is the continuous wavelength coverage from the near- to mid-IR (2–24 μm), especially at 11 and 15 μm, which allows detecting the MIR-excess dust emission from circumstellar matter around AGB stars. Therefore, *AKARI* observations are well suited for the study of MIR excess from AGB stars, as well as obscured SFA. The ANWS covers intermediate- and low-density regions at $0.07 < z < 0.1$ where the NEP supercluster is located. To compare the galaxy properties in these regions with those in high-density regions, we include the galaxy data of A2255 that was also observed by *AKARI* as part of the mission program of CLusters of galaxies EVoLution studies (CLEVL; Im et al. 2008; Lee et al. 2009b). The *AKARI* observations for the A2255 field were carried out using six InfraRed Camera (IRC) filters (Shim et al. 2011). The depth of the A2255 data is comparable to that of the ANWS. Thus, the uniformity of our *AKARI* IR data across a range of environments (a rich cluster, three groups, and lower density regions) allows us to directly investigate the galaxy populations and their environmental dependence.

The primary goal of this study is to understand how environment and mass affect the evolution of galaxies, focusing on the quenching of the SFA, and morphological transformation. To do this, we focus on transition populations (red-sequence galaxies with various MIR properties), taking advantage of the multi-wavelength (UV-to-MIR) data for galaxies in the NEP supercluster at $0.07 < z < 0.1$. Most importantly, the 11 μm flux traces not only the mean stellar age and the specific SFR (SSFR) of SF galaxies but also the presence of intermediate-age stellar populations, detecting even tiny amounts of past star formation in early-type galaxies.

Throughout this paper, we use $H_0 = 70$ km s^{-1}Mpc^{-1}, $\Omega_M = 0.3$, and $\Omega_\Lambda = 0.7$. In this cosmology, an angular scale of 1 arcsec at the distance of the NEP supercluster corresponds to 1.629 kpc. All magnitudes are given in the AB system.

2. THE DATA

2.1. IR and Optical Imaging

The ANWS was carried out using all available filters of the IRC. For each of the *AKARI* cameras, there are three associated channels: NIR (N2, N3, and N4), MIR-S (S7, S9W, and S11), and MIR-L (L15, L18W, and L24), all with a field of view covering $10' \times 10'$. The numbers next to each letter represent the central wavelengths in μm, and the W's for 9 and 18 μm represent the wider bandwidths. The ANWS was completed with 446 pointed observations covering a large area of $\sim$5.4 deg^2 toward the NEP. Each pointing was done with the "IRC03" Astronomical Observation Template (AOT; see AKARI Observer's Manual version 1.2[12]), with two dithered pointings per filter. For detailed descriptions of the survey strategy, its observational properties, and the reduction of the *AKARI* IR images we refer the reader to Matsuhara et al. (2006) and Lee et al. (2009a).

The optical survey covers the ANWS field centered at $\alpha = 18^{h}00^{m}00^{s}$, $\delta = +66°36'00''$. The central 2 deg^2 were covered by the Canada–France–Hawaii Telescope (CFHT) Megacam u^*, g', r', i', and z' filters (Hwang et al. 2007). The remaining area (which includes a small overlap with the CFHT Megacam data) is covered with the SNUCAM (Im et al. 2010) on the 1.5 m telescope at Maidanak Observatory in Uzbekistan using the Bessell B, R, and I filters (Jeon et al. 2010). We convert the CFHT Megacam (of ANWS) and SDSS (of A2255) photometry into the photometric system of Maidanak (i.e., Bessell B and R) using best-fit SED model colors. In the following analysis, the final uncertainties combine (in quadrature) the original photometric errors with the uncertainties derived from the SED fits, which are typically <0.1 mag.

NIR imaging was also carried out using FLAMINGOS on the KPNO 2.1 m telescope, which covers 5.2 and 5.4 deg^2 in the J and H bands, respectively. Figure 1 shows the coverage of each survey, and the mean depth and the FWHM of each band are summarized in Table 1. We did not use the *AKARI* L24 data in this study due to its insufficient sensitivity. The photometry has been corrected for foreground Galactic extinction using the Schlegel et al. (1998) dust maps and Cardelli Milky Way extinction curve (Cardelli et al. 1989), assuming $R_V = 3.1$.

The object detection and photometry was done with SExtractor (Bertin & Arnouts 1996) on the co-added images of each individual band. We consider sources as real detections if they have more than five contiguous pixels above 3 $\times$ the rms fluctuations of the sky. However, it was necessary to match the *AKARI* objects with optical counterparts (FWHM of 0.″8–1.″4) due to the low resolution (FWHM of 5.″5–6.″6) of *AKARI* images. Thus, sources that SExtractor cannot separate properly because of blending with neighbors in the *AKARI* IR images are excluded. The photometry was done using SExtractor in a

[12] http://www.ir.isas.jaxa.jp/ASTRO-F/Observation/ObsMan/akobsman12.pdf

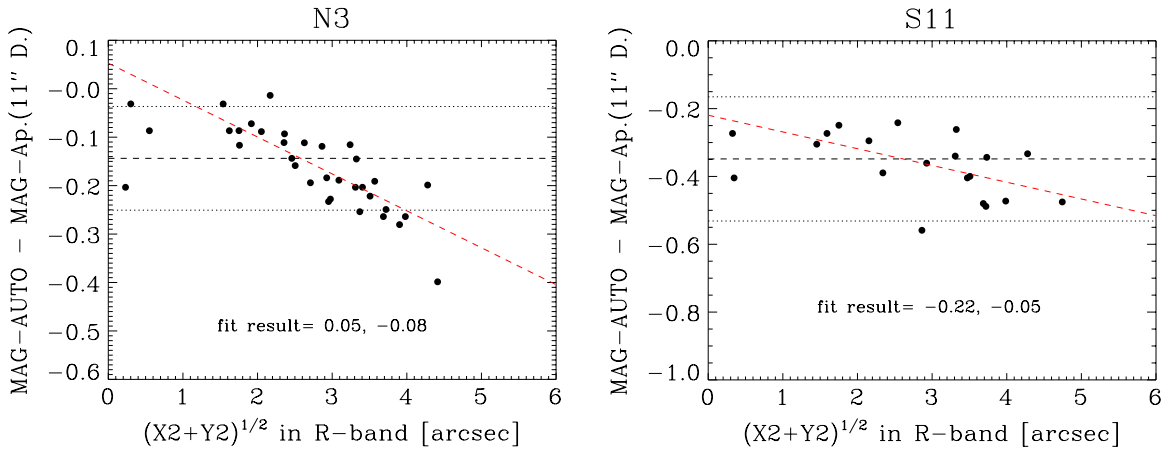

Figure 2. Second-order moments (from SExtractor) in the Maidanak *R*-band image vs. magnitude difference between MAG-AUTO and MAG-APER with 11″ diameter for N3 (left) and S11 (right). To determine aperture correction factors, we used the best fit (red dashed lines) for galaxies which are not contaminated by nearby objects. Black dashed and dotted lines show the mean value and the standard deviation of all sample galaxies in N3 (left) and S11 (right), respectively.

(A color version of this figure is available in the online journal.)

Table 1
The Imaging Data Set in the ANWS

Covering Area	CFHT					Maidanak			KPNO		*AKARI*							
	2 deg^2					4.9 deg^2			5 deg^2		5.4 deg^2							
Band	u^*	g'	r'	i'	z'	B	R	I	J	H	N2	N3	N4	S7	S9W	S11	L15	L18W
Depth (AB mag.)	26.0	26.1	25.6	24.7	23.7	23.2	22.0	21.2	20.5	19.3	20.9	21.1	21.1	19.5	19.3	19.0	18.6	18.8
FWHM (arcsec)	1.13	1.05	0.93	0.84	0.79	1.4	1.2	1.1	1.4	1.3	5.5	6.0	6.0	5.9	6.6	5.9	6.2	6.2
	(1)	(2)	(3)	(4)	(5)	(6)	(7)	(8)	(9)	(10)	(11)	(12)	(13)	(14)	(15)	(16)	(17)	(18)

Notes. Columns 1–5: CFHT Megacam u^*, g', r', i', and z' from Hwang et al. (2007); Columns 6–8: Maidanak *B*, *R*, and *I* from Jeon et al. (2010); Columns 9 and 10: KPNO FLAMINGOS *J* and *H* from Y. Jeon et al. (2012, in preparation); Columns 11–18: *AKARI* N2, N3, N4, S7, S9W, S11, L15, and L18W from Lee et al. (2009a).

single-band mode, and we used MAG-AUTO for the total magnitudes. To check the MAG-AUTO values we performed large-aperture photometry for several isolated galaxies in the final image. These showed that the difference between MAG-AUTO and MAG-APER were smaller than the typical measurement errors (NIR: $\leqslant 5\%$; MIR: $\leqslant 20\%$). However, MAG-AUTO for sources with close neighbors can easily be contaminated by them. To derive fluxes of such objects, we used the aperture photometry and applied aperture corrections that are derived from the relation between second-order moments (SExtractor parameters for measuring the width of the point-spread function) of the Maidanak *R* band or CFHT r' band and the 11″ ($\sim$2 $\times$ FWHM) diameter aperture flux. Figure 2 shows the relation between the second-order moments for isolated galaxies in the Maidanak *R*-band image and the magnitude difference between MAG-AUTO and MAG-APER for N3 and S11. To determine the aperture correction factors, we used the best fit (red dashed lines) for sample galaxies that are not contaminated by nearby sources.

2.2. Optical Spectroscopy

The spectroscopic follow-up of galaxies in the ANWS field used MMT/Hectospec and WIYN/Hydra. Based on the optical and IR fluxes, we selected objects with power-law SEDs as active galactic nucleus (AGN) candidates (N2 $-$ N4 $>$ 0 and S7 $-$ S11 $>$ 0; see Lee et al. 2007) and S11-detected objects with 15 μm flux brighter than 250 μJy as SF galaxy candidates. Supercluster member candidates (red-sequence galaxies) were selected using the NIR color–magnitude diagram ($-0.7 <$ N3 $-$ N4 < -0.4) and a brightness requirement in the N2 band (N2 $<$ 18). This color cut is adopted as a rough cluster member selection criterion based on the *AKARI* study of A2255 galaxies that are at a similar redshift (Shim et al. 2011). We also visually inspected the *R*- or r'-band images to exclude stars. In summary, we selected as spectroscopic targets galaxies with a wide range of IR fluxes to study their IR properties in a variety of local density environments. However, because of signal-to-noise limitations, identifying the correct redshifts of faint absorption-line galaxies is often very difficult, so that less massive galaxies with absorption-line spectra are underrepresented in the sample. We took into account this incompleteness in our analysis.

2.2.1. MMT Hectospec Observations

Hectospec is a multiobject, moderate-dispersion spectrograph, covering a 1° diameter field of view at the $f/5$ focus of the 6.5 m MMT (Fabricant et al. 2005). It comprises 300 fibers of 1.″5 diameter, covering a wavelength range of 3500–9000 Å with 6 Å FWHM resolution.

The Hectospec observations are taken in queue mode, so that the field is targeted when optimally placed on the sky. A total of five configurations were obtained between 2008 May and November. A log of the observations is shown in Table 2, which contains the field identification, the J2000.0 coordinates, total exposure time, and date.

The Hectospec observations used a catalog of galaxies detected in the *AKARI*-IR bands (high-priority objects), complemented by other galaxies with $R \leqslant 22$ in the region, but that were undetected by *AKARI*. In addition to galaxies, this catalog also contains candidate F stars, selected from the photometry, which are used to flux-calibrate the spectra. The assignment of objects

Table 2
MMT Hectospec Fields

Field	R.A. (J2000)	Decl. (J2000)	t_{exp} (minutes)	Observation Date (UTC)
nep-hecto-1	17 54 50.66	+66 38 47.48	100	2008 May 3
nep-hecto-2	18 04 29.63	+65 53 32.20	80	2008 Jun 2
nep-hecto-3	17 55 09.27	+65 49 28.81	80	2008 Sep 3
nep-hecto-4	17 59 29.51	+67 16 03.83	80	2008 Nov 17
nep-hecto-5	18 07 39.24	+66 38 56.78	80	2008 Nov 20

Table 3
WIYN Hydra Fields

Field	R.A. (J2000)	Decl. (J2000)	t_{exp} (minutes)	Observation Date (UTC)
NEP00	18 00 10.031	+66 34 00.00	80	2008 Jun 27
NEP01	17 56 29.855	+66 21 00.00	80	2008 Jun 27
NEP02	17 54 09.796	+65 54 00.00	100	2008 Jun 27
NEP03	17 51 51.806	+66 16 00.00	80	2008 Jun 28
NEP04	17 52 58.195	+66 58 00.00	80	2008 Jun 28
NEP05	17 54 51.441	+67 10 00.00	60	2008 Jun 29
NEP06	17 59 28.904	+67 16 00.00	60	2008 Jun 30
NEP07	18 05 22.322	+67 10 00.00	60	2008 Jun 30
NEP08	18 09 25.763	+66 59 00.00	60	2008 Jun 30
NEP09	18 08 18.026	+66 20 00.00	60	2008 Jun 30

to fibers is done using XFITFIBS,[13] which takes into account the number of configurations (five in the case of the ANWS), the object priorities, and the number of sky positions. Typically 250 fibers per setup were assigned to NEP objects, 40 to random sky positions and up to 6 fibers placed on the candidate F stars. The spectroscopic reduction used the *HSRED* package of *IDL* scripts written by R. Cool,[14] which is based on the *IDL* pipeline developed for the reduction of SDSS spectra. *HSRED* does the standard reduction by correcting for bias, flat fields, illumination (if twilight flats were taken), performing wavelength calibration (from HeNeAr lamps), sky subtraction, and extracting one-dimensional spectra. The flux calibration is done by combining the one-dimensional F-star spectra with the multiband photometry (to obtain the spectro-photometric zero point) and Kurucz stellar models (to rectify the spectra). Redshifts for the wavelength- and flux-calibrated spectra are obtained from the cross-correlation with a series of galaxy, QSO, and stellar template spectra. All Hectospec redshifts were individually validated and assigned a quality code ranging from 1 to 4, as used for the DEEP2 survey (e.g., J. A. Newman et al. 2012, in preparation; Willmer et al. 2006). Only qualities of 4 or 3 are used in the analyses, meaning that the probability of the redshift being correct is greater than 95% and 90%, respectively.

2.2.2. WIYN Hydra Observations

We also obtained optical spectra with the Hydra multiobject spectrograph on the WIYN 3.5 m telescope at Kitt Peak National Observatory. We used 98 red fibers of 2″ diameter feeding the bench spectrograph with a 316 lines mm^{-1} grating, yielding a dispersion of 2.64 Å pixel^{-1}. The wavelength range is 4500–9000 Å, but the spectrum quality is low beyond 8000 Å due to the strong sky emission lines. The field of view of Hydra is approximately 1° and we observed ten fields over the ANWS field (Figure 3).

[13] http://www.harvard.edu/john/xfitfibs
[14] http://www.astro.princeton.edu/rcool/hsred/hsred/reductions.html

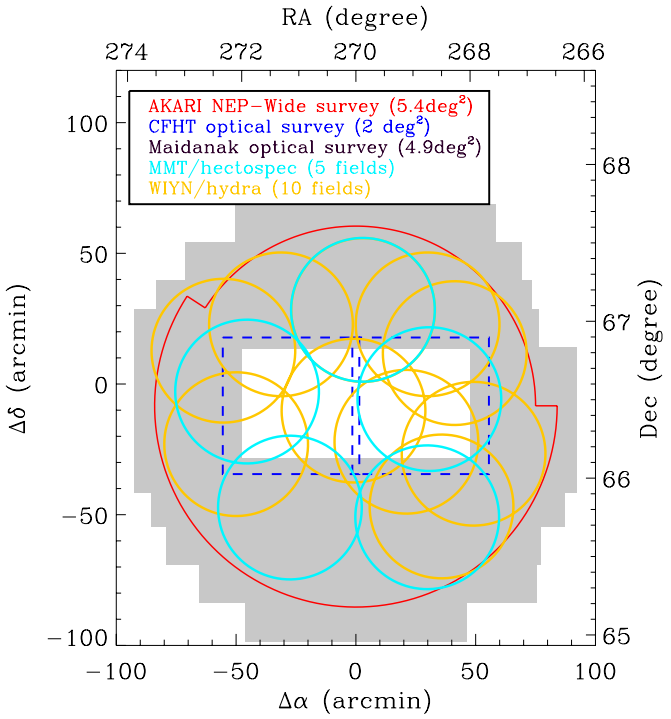

Figure 3. Follow-up spectroscopic observations of the NEP-Wide survey. The five cyan circles indicate MMT/Hectospec fields, and the ten yellow circles indicate WIYN/Hydra fields. The representation of the *AKARI* and optical surveys are the same as in Figure 1.
(A color version of this figure is available in the online journal.)

Target assignment in each configuration was done using the WHYDRA software. For each configuration, 10–15 fibers were assigned to blank sky positions, and 3–6 fibers were assigned to spectrophotometry standard stars. Excluding broken fibers, fibers assigned to blank sky positions, and fibers assigned to standard stars, we obtained spectra of 60–70 targets in each configuration. In Figure 3, the locations of the Hydra configurations are shown by ten yellow circles, and details of the observations are summarized in Table 3. Depending on the observing conditions, the exposure time for each field varied from 3 × 20 minutes to 5 × 20 minutes.

We used IRAF to reduce the spectra. First, we performed the pre-processing that includes the corrections for overscan, bias, dark and flat, and trimming the image. A flat-field image was created by averaging dome flats taken before and after the observations. We removed cosmic rays using L.A.Cosmic (van Dokkum 2001). After the pre-processing, we extracted one-dimensional spectra using the Hydra reduction package DOHYDRA (Valdes 1995). We extracted one-dimensional spectra from all apertures and did wavelength calibration with a Cu–Ar comparison lamp. The master sky spectrum produced by co-adding sky spectra of blank skies was subtracted with DOHYDRA. Finally, the extracted one-dimensional spectral images were combined using IRAF task *scombine* to improve the final signal-to-noise ratio.

2.2.3. Redshift Identification

Redshifts were determined by identifying high signal-to-noise emission lines and/or multiple absorption lines. Three individuals (J. Ko, M. Im, and H. Shim) independently determined redshifts for all objects. Then, each of them flagged objects according to their spectral features. We flagged the objects with at least two distinct spectral features as those with

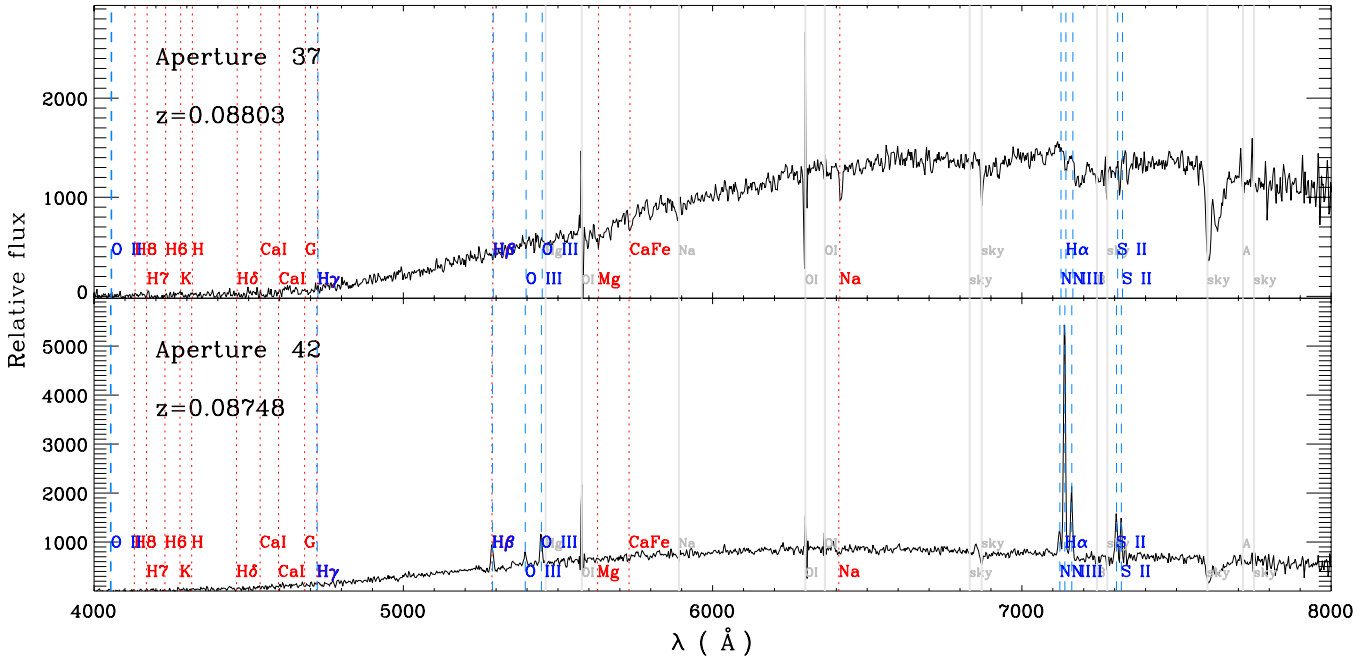

Figure 4. Sample of WIYN/Hydra spectra with sky (gray), absorption (red), and emission (blue) lines used for redshift determination. (A color version of this figure is available in the online journal.)

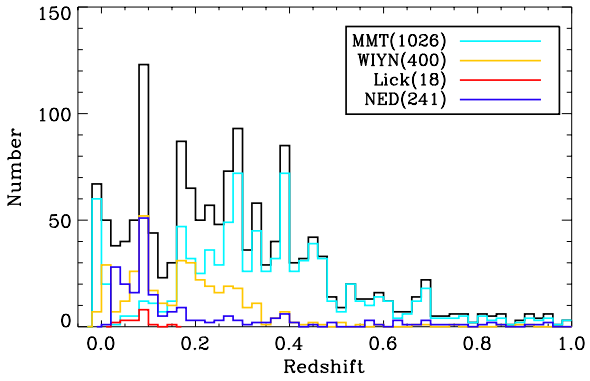

Figure 5. Redshift distribution of galaxies with secure redshifts in the ANWS. The black line shows the redshift distribution of the total spectroscopic sample. (A color version of this figure is available in the online journal.)

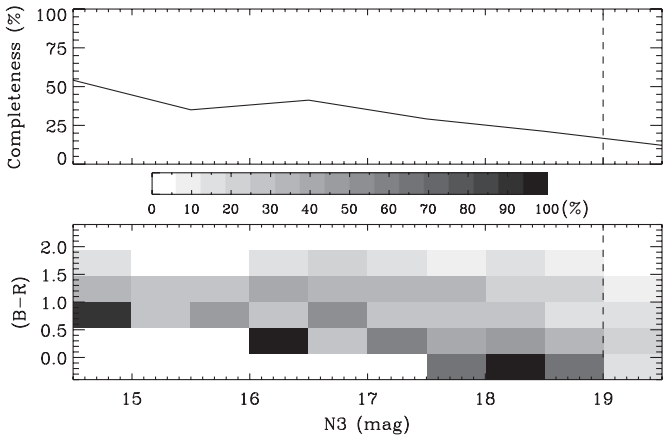

Figure 6. Spectroscopic completeness as a function of the N3 apparent magnitude (top panel) and observed $(B-R)$ color and N3 apparent magnitude (bottom panel) of galaxies in the ANWS. Vertical dashed lines indicate the N3 magnitude cut used in this study.

a secure redshift. All individuals generally agree on the secure redshifts, but faint or distant galaxies can be ambiguous due to the weak line features. These objects were not used in the analyses.

To verify our redshift determination, we ran *XCSAO* in the *RVSAO* package, which computes radial velocities by cross-correlating spectra against templates of known redshift (Kurtz et al. 1992). In this test, we used 61 supercluster member galaxies flagged as having secure redshifts with Hectospec galaxy templates and found that the difference of radial velocities for all samples is 119 ± 123 km s^{-1}, consistent with no difference in radial velocities measured from both methods and telescopes.

We were able to successfully determine secure redshifts for 1026 and 400 of 1195 Hectospec objects and 600 Hydra objects, respectively. Figure 4 shows a sample of WIYN spectra with lines used to determine redshifts, and the redshift distribution of all objects with secure redshifts in the ANWS is shown in Figure 5. To this sample we added 241 galaxies for which redshifts are available in the NASA Extragalactic Database (NED). An additional 18 redshifts come from long slit spectra obtained by Matthew Malkan using the Kast spectrograph at the Lick Observatory 3 m telescope.

In Figure 6, we plot the spectroscopic completeness as a function of the observed N3 magnitude and $(B-R)$ color for extended sources. Here we use the N3 band and $(B-R)$ color because we will adopt the absolute N3 band as a rough stellar mass indicator and $(B-R)$ color to separate red-sequence galaxies from blue-cloud galaxies. The vertical line represents our N3 magnitude cut (N3 < 19) used in this study.

2.3. Supercluster Member Selection

The sample of NEP supercluster members used in this paper consists of the spectroscopic sample of galaxies at $0.07 < z < 0.1$ in the field of ANWS and of galaxies in A2255 (see Figure 7).

After removing duplications, we have a total of 150 secure spectroscopic objects in the redshift interval $0.07 < z < 0.1$

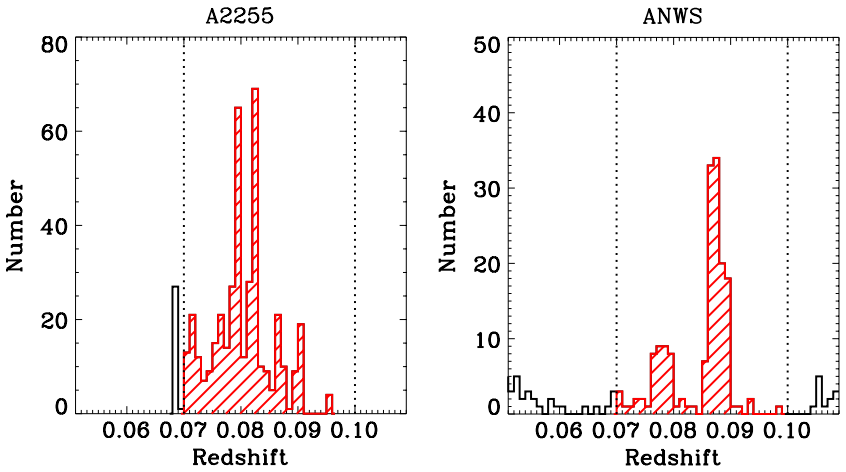

Figure 7. Redshift distribution of galaxies in A2255 (left) and the ANWS (right). The vertical dotted lines indicate the redshift range of the NEP supercluster ($0.07 < z < 0.1$).

(A color version of this figure is available in the online journal.)

in the ANWS. Using the optical positions, we matched the spectroscopic data with catalogs derived from our *AKARI* IR data, KPNO NIR data (*J* and *H*), and *Galaxy Evolution Explorer* (*GALEX*) UV data where available. The matching radius was chosen to be 5.0 arcsec. All matched objects were then visually validated by examining postage stamp images for all bands.

The A2255 spectroscopic and photometric data are drawn from Shim et al. (2011). We used 313 objects covered by the *GALEX* UV data. The redshift identification is nearly complete for galaxies with $r < 18.9$ mag. The limiting optical magnitude places a limit in the derived infrared luminosity, which will be taken into account in the following analysis. As for the ANWS data, the redshift range for NEP supercluster member galaxies is $0.07 < z < 0.1$. The detection limits for the observed bands are 25, 30, 65, 80, 150, and 400 μJy in the N3, N4, S7, S11, L15, and L24 bands, respectively (Shim et al. 2011). The depth of the A2255 data is comparable to that of the ANWS data within the measurement errors.

3. PHYSICAL PROPERTIES

In this section, we describe the method used to derive the galaxy stellar masses, SFR, and local galaxy density.

3.1. Spectral Energy Distributions

We derive the stellar mass, the mean stellar age, the reddening parameter, and the SFR for each object through SED fitting, which uses a standard χ^2 minimization procedure with various templates. We used two different SED libraries—the Bruzual & Charlot (2003; BC03) spectral synthesis models to estimate the stellar mass and age, and the IR templates of SF galaxies from Chary & Elbaz (2001; CE01) to determine the IR luminosity. When performing the fits for SF galaxies, we only use the IR data in the fits, as the empirical IR templates do not include the diverse range of ages, metallicities, and star formation histories that are modeled by the BC03 library. Figure 8 shows examples of the observed UV–optical–MIR SEDs of galaxies in the ANWS, and the best-fit SEDs from each model are overplotted.

Stellar masses were estimated using stellar population synthesis models (e.g., Bell et al. 2003; Ilbert et al. 2010). During the SED-fitting process, the redshift was kept fixed, and all bands from the NUV to NIR (NUV–N4) were used to fit a purely stellar SED. The SED templates were generated with BC03 models assuming a Chabrier (2003) initial mass function (IMF) and an exponentially declining star formation history SFR $\propto e^{-t/\tau}$ (τ between 0.1 Gyr and 30 Gyr). The SEDs were generated for a grid of 44 ages (0.1–13.5 Gyr) and three different metallicities (0.02, 0.008, and 0.004 $Z_\odot$), and dust extinction was added using the formula of Calzetti et al. (2000) for E_{B-V} between 0 and 0.5. Figure 9 shows the stellar masses computed with BC03 versus the N3 absolute magnitude of galaxies in the ANWS, which shows a good correlation. This suggests that N3 is a rough indicator of the stellar mass. As $M_{\rm N3} = -19$ corresponds to a stellar mass of $\sim\log M_* = 9.1\,M_\odot$, the stellar mass range of our sample is roughly $\log M_* = 9.1$–$11.5\,M_\odot$. The histogram of the N3 absolute magnitude of galaxies is shown in the upper panel of Figure 10, where the top axis shows stellar masses corresponding to the N3 absolute magnitude (Figure 9).

To derive the $L_{\rm IR}$ for each galaxy, we use the IR templates of CE01. Templates are shifted to each galaxy's redshift and then matched to all the available bands longer than 7 μm (i.e., the *AKARI* S7, S9W, S11, L15, and L18W bands). We first subtract the stellar contribution (i.e., the best-fit BC03 template to the UV–NIR data) from the observed IR data, and then fit them with CE01 templates to estimate the total IR luminosity at 8–1000 μm ($L_{\rm IR}$). We convert $L_{\rm IR}$ into SFR using the Kennicutt (1998) relation: SFR $(M_\odot\,{\rm yr}^{-1}) = 1.72 \times 10^{-10}\ L_{\rm IR}/L_\odot$. The lower panel of Figure 10 shows the distribution of derived total IR luminosity $L_{\rm IR}$ for S11-detected galaxies. We only find two luminous IR galaxy (LIRG; $\log L_{\rm IR}/L_\odot > 11$) candidates in the ANWS field. Conservatively, we estimate an SFR limit of $0.1\,M_\odot\,{\rm yr}^{-1}$ in A2255 and $0.2\,M_\odot\,{\rm yr}^{-1}$ in the ANWS. There is a likely contribution of AGN to the IR luminosity. However, the contamination in our sample is very low if we assume many AGNs have power-law IR SEDs (e.g., Lee et al. 2007). Among the supercluster member galaxies in the ANWS, there is only one X-ray point source (detected by *ROSAT*), which is also an LIRG. Thus, AGN contamination is expected to be negligible in our results.

3.2. Galaxy Local Density

Although our data set does not cover the entire NEP supercluster, it covers a wide range of environments, including a rich galaxy cluster (A2255), three galaxy groups, and low-density regions in the supercluster outskirts.

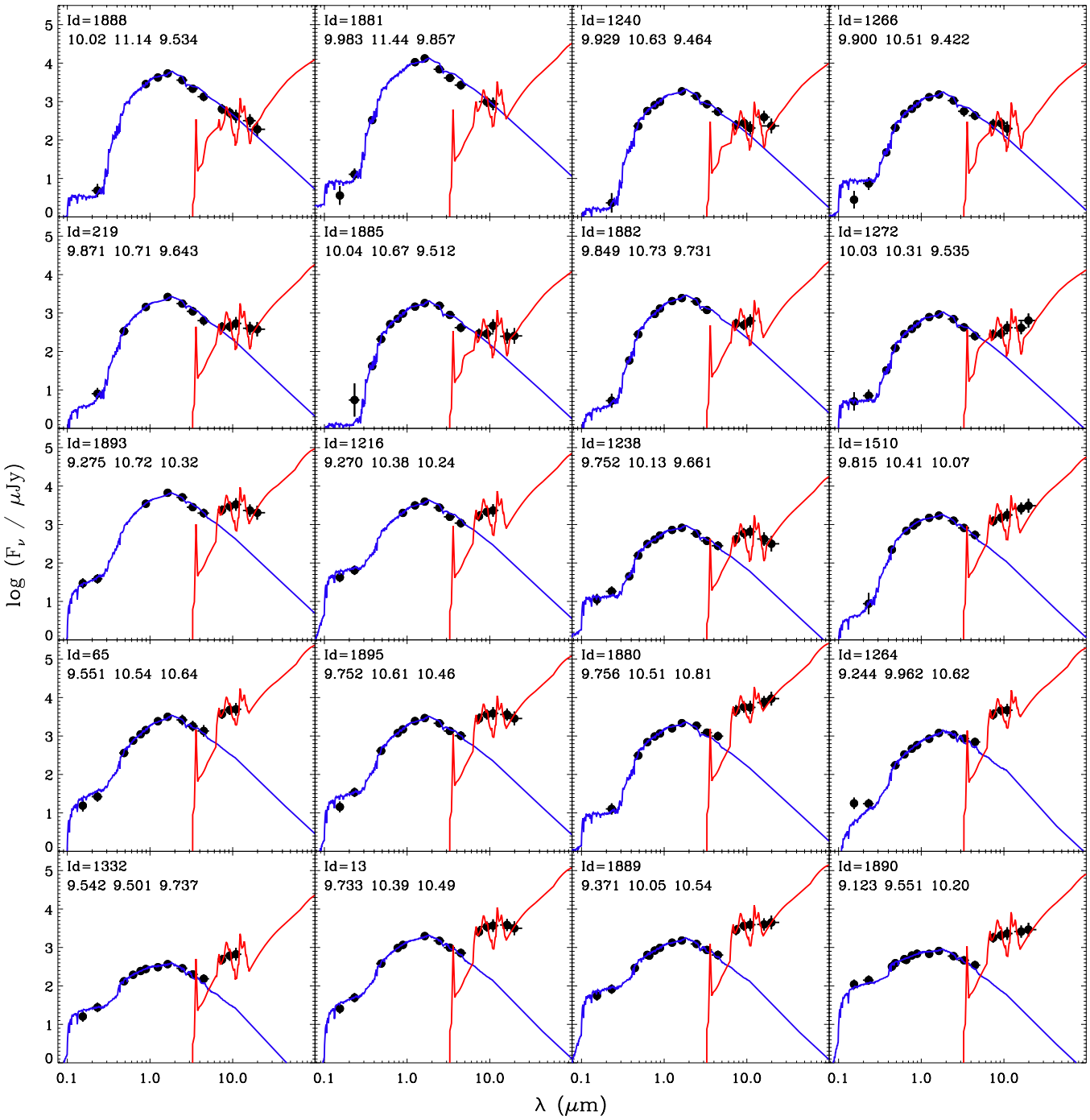

Figure 8. Examples of the SEDs of galaxies in the ANWS. Filled circles indicate observed data points from *GALEX* UV to *AKARI* MIR. All objects are detected in S11, except in cases where objects were not detected in the *AKARI* L15 and L18 bands (Id: 1881, 1266, 1882, 1216, 65, 1264, and 1332), in which cases no points are shown. Overplotted lines represent the best-fit SEDs: the blue solid lines indicate SEDs from Bruzual & Charlot (2003) and the red solid lines indicate infrared galaxy templates of Chary & Elbaz (2001). Each SED fit lists the object Id on top left; stellar age (years), stellar mass ($M_\odot$), and total $L_{\rm IR}$ ($L_\odot$) in units of dex, from left to right, respectively. Each row shows a set of four objects that are representative of our classification scheme (described in Table 4): weak-MXG, intermediate-MXG, weak-SFG, dusty-SFG, and blue-SFG, from top to bottom.

(A color version of this figure is available in the online journal.)

To characterize the galaxy properties as a function of the environment, we adopt a local surface density estimator Σ, which is the surface number density of galaxies within a projected distance of 0.5 Mpc and within a relative velocity of 1000 km s^{-1} for each galaxy in the sample. The velocity cut is adopted to exclude foreground and background galaxies. Our method of measuring galaxy environment (i.e., the fixed aperture environment measure) is found to be the best estimate of galaxy environmental density when the virial radius of the host halo is difficult to measure according to Haas et al. (2012), so we chose this as our density parameter for discussion. As a cautionary measure, we compared several other environment indicators against this measure, using galaxies in A2255. Two other indicators are tested, one is the surface number density of galaxies within a projected distance of 1.0 Mpc and within a relative velocity of 1000 km s^{-1} ($\Sigma_{1.0\,\rm Mpc}$), and another is the

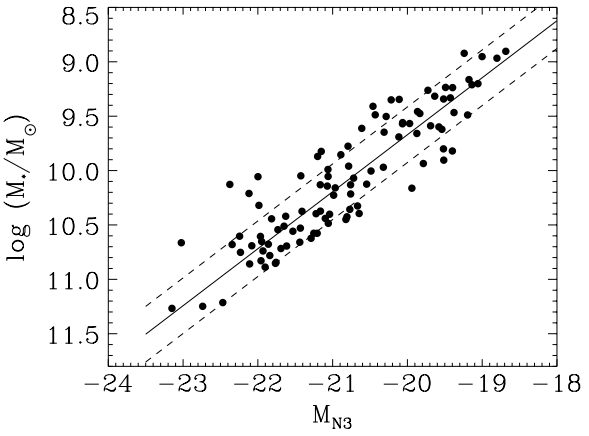

Figure 9. Stellar masses computed with BC03 vs. the N3 absolute magnitude of galaxies in the ANWS. Here we used 102 galaxies for which five or more bands were used in the SED fits. The solid line indicates the best fit ($\log M_*/M_\odot = -0.524 \times M_{N3} - 0.810$), and the two dashed lines represent the standard deviation of residuals to this fit ($\sigma = 0.255$).

surface number density of galaxies within a projected distance to the 5th-nearest neighbor and within a relative velocity of 1000 km s^{-1} ($\Sigma_{5\text{th}-\text{nearest}}$). In the right panel of Figure 11, we show the correlation between the local density adopted in this work ($\Sigma_{0.5\,\text{Mpc}}$) and other environmental parameters. The Spearman rank correlation coefficient is also printed, indicating that other choice of environmental parameters correlates well with our choice. Indeed, we performed the analysis on our main results using these different environment parameters and found that the results are not affected by a choice of the environmental parameter. To account for the spectroscopic incompleteness of the NEP-Wide survey, the number density is computed by weighing each galaxy by the inverse of completeness corresponding to its N3 apparent magnitude and $(B-R)$ color in Figure 6. The left panel of Figure 11 shows the distribution of the local surface density for galaxies in A2255 (dotted line) and in the ANWS (dashed line). The peak density in the ANWS area corresponds to the lowest density region of A2255, i.e., the infall region of A2255. We refer to this as an intermediate local density in the following analysis. The spatial distribution of all supercluster member galaxies in A2255 and in the ANWS field is overplotted on their number density map in Figure 12.

4. GALAXY CLASSIFICATIONS: MIR VIEW OF GALAXIES

4.1. Motivation

The optical CMR is commonly used to separate red-sequence (hereafter red) galaxies from blue-cloud (hereafter blue) galaxies. Blue optical colors can mean that galaxies are actively SF. While the presence of an AGN can make a galaxy blue (e.g., Obrić et al. 2006; Choi et al. 2009b), SF is in general the cause of blue galaxy colors. The red colors of galaxies can be due to a dominant population of passively evolving old stars (even though some galaxies with predominantly old stars have low-level SF; e.g., Trager et al. 2000). Galaxies can also be red in the optical/NUV if their light is extinguished by interstellar dust. Thus, we need to differentiate such causes of red galaxy colors.

We show the CM diagram of A2255 galaxies (the left side of Figure 13) compared to galaxies in the ANWS (the right side of Figure 13) in three colors: $B-R$ (panels (a) and (d)), NUV $-$ R (panels (b)and (e)), and N3 $-$ S11 (panels (c)and (f)). The absolute N3 magnitude (horizontal axis) is used as a rough measure of the stellar mass (see Figure 9). To determine the rest-frame M_{N3} absolute magnitude, we apply only the luminosity distance of each galaxy (i.e., no correction for peculiar motions or bandpass shift is included). In the following analysis, we only consider galaxies brighter than $M_{N3} = -19$ (corresponding N3 $\approx$ 19) due to the relatively shallow S11 detection limit. Specifically, this cut allows us to construct an unbiased sample of galaxies with N3 $-$ S11 > 0 (see the next section).

In Figures 13(a) and (d), we show the $B-R$ optical CMR for galaxies brighter than $M_{N3} = -19$ in A2255. The red sequence is defined using a linear fit to the observed $B-R$ versus M_{N3}, shown as a dashed line, by rejecting outliers iteratively based on the bi-weight calculation. The standard deviation of residuals to the fit is 0.07 mag (σ), implying a tight optical red sequence. The horizontal solid line indicates the color cut we adopted to separate red galaxies (redward of the solid line) from blue galaxies (blueward of the solid line). The CMR was moved to a bluer color by $\Delta(B-R) = 0.21(\sim 3\sigma)$ to define the color cut. The same color criterion is applied to the galaxies in the ANWS.

Figures 13(b) and (e) show the NUV $-$ R CM diagram for the same sample as in panels (a) and (d). The NUV CM diagram shows a scatter an order of magnitude larger than that in the optical data, indicating that a number of red galaxies have been forming stars (e.g., Yi et al. 2005). Since the NUV flux is much more sensitive to young stellar populations than the optical flux, it can be a good tracer of recent star formation (within $\sim$1.5 Gyr). However, while the NUV flux is also sensitive to dust extinction, the MIR flux is not. The wide dispersion in the N3 $-$ S11 colors for red galaxies in the MIR CM diagram (Figures 13(c) and (f)) suggests that these galaxies present a variety of MIR properties.

We focus in particular on the MIR. The choice of the S11 band has several advantages over other MIR bands. First, the S11 flux correlates with the PAH emission features at 11.3 and 12.7 μm, which may be related to current star formation. Because of the PAH features, MIR emission (especially around 11 μm) correlates well with the total IR luminosity (Spinoglio et al. 1995), which can be converted into SFR (Chary & Elbaz 2001). Second, the MIR emission may also contain a contribution from the envelopes of evolved stars, showing broad silicate emission features around 10 μm (e.g., Bressan et al. 2006) or/and unusual PAH features (e.g., Vega et al. 2010). In particular, this MIR emission from dust surrounding AGB stars is also sensitive to stellar ages because it declines with time (e.g., Piovan et al. 2003; Temi et al. 2005). Thus, the MIR emission may be tracing not only the current SF but also past SFA. For the model SEDs in Figure 13(c), we used Single Stellar Population (SSP) models including the dust emission from circumstellar dust around AGB stars (Piovan et al. 2003; hereafter P03). As has been recognized, the optical CMR can be well described with a single age model assuming a metallicity gradient (the dashed line in Figure 13(a); e.g., Kodama & Arimoto 1997). The same model fits the N3 $-$ S11 versus N3 CMR at three different stellar ages (1, 5, and 12 Gyr), shown by dotted lines. The horizontal solid line represents the SSP model without AGB dust. However, any single age model fails to reproduce the dispersion in the N3$-$S11 colors (see Ko et al. 2009), which suggests either the existence of younger stellar populations or of some other mechanism.

We divide the red galaxies into several subsamples with different SFA by using the N3 $-$ S11 colors. We note that

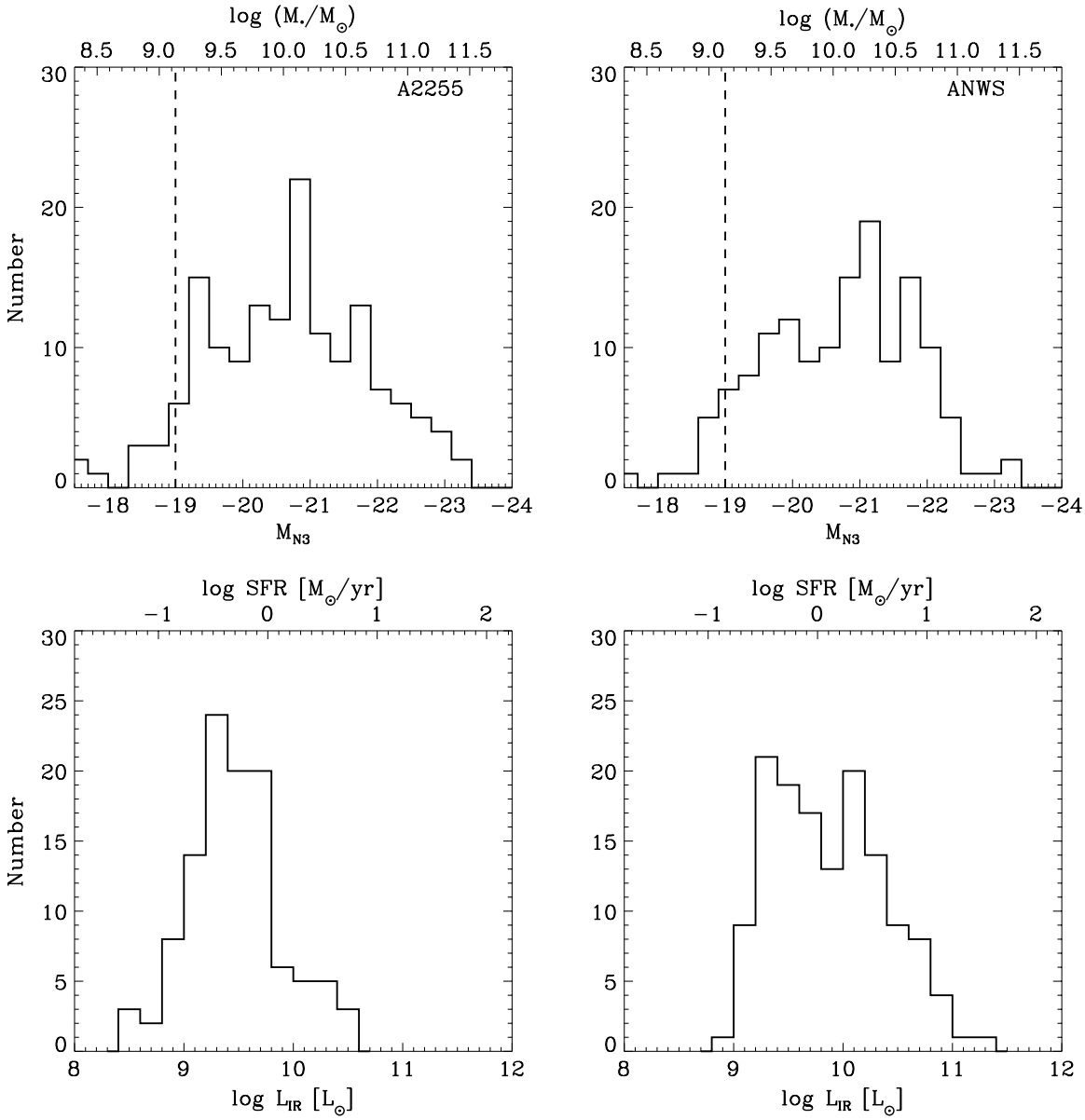

Figure 10. Upper: histogram of the N3 absolute magnitude of galaxies in A2255 (left) and in the ANWS (right). The top axis shows stellar masses calculated from the linear relation in Figure 9. Vertical lines are our N3 magnitude cut. Lower: distribution of derived total IR luminosity $L_{\rm IR}$ (8–1000) for S11-detected galaxies in A2255 (left) and the ANWS (right). The top axis corresponds to SFR, using the Kennicutt (1998) relation.

NIR–MIR color can be considered as an indicator of the SSFR (SFR/M_*) of SF galaxies, and also of the luminosity-weighted mean stellar age in passively evolving objects.

4.2. MIR Classification

Using the *Spitzer* Wide-area InfraRed Extragalactic (SWIRE) survey templates of Polletta et al. (2007), we find that early-type galaxies (e.g., ellipticals, S0, and Sa) have N3 − S11 < 0, while SF, late-type galaxies have N3 − S11 > 0 (see Figure 14). These templates have been successfully used in a number of works for all galaxy types at a range of redshifts (e.g., Adami et al. 2008; Ilbert et al. 2009). Among the SWIRE templates, we use 16 templates including 3 ellipticals (with 2, 5, and 13 Gyr), 7 spirals, and 6 starbursts covering the wavelength range between 0.1 and 1000 μm. These are generated with the GRASIL code (Silva et al. 1998) including dusty envelopes of AGB stars following the prescription by Bressan et al. (1998). In particular, in the MIR spectral region between 5 and 12 μm, the spiral and starburst templates encompass the variety of observed MIR spectra (Polletta et al. 2007). Also shown as a comparison are SSP templates of P03 incorporating AGB dust with a metallicity ($Z = 0.02$) and three stellar ages (2, 5, and 13 Gyr). The P03 model SEDs show somewhat redder N3 − S11 colors than the GRASIL model due to a difference in how dust emission from evolved stars is predicted, but they are broadly in agreement that N3 − S11 color as the mean stellar age decreases. For comparison, we also plot SSPs from different libraries (BC03, CB07, and Ma05) with a Salpeter (1955) IMF and a fixed metallicity ($Z = 0.02$), but without the inclusion of the MIR dust emission prescription. CB07 is a new version of BC03 including the new stellar evolution prescription of Marigo & Girardi (2007) for the thermally pulsing (TP) AGB evolution, and Ma05 is also including the TP-AGB phase of stellar evolution (Maraston 2005) differently from previous models. However, these two SSPs (CB07 and Ma05) do not

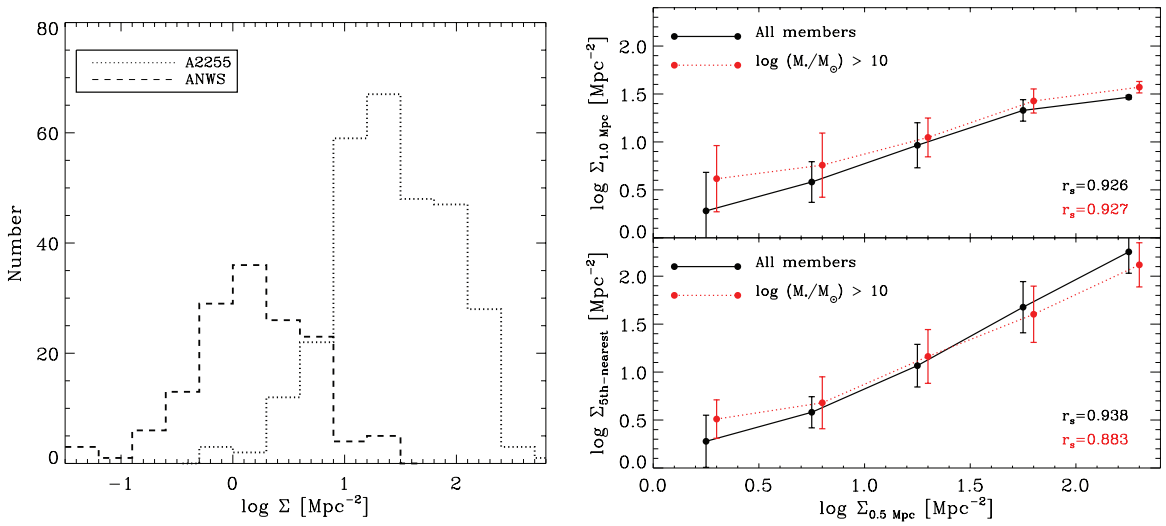

Figure 11. Left: distribution of the local density Σ for galaxies in A2255 (dotted line) and in the ANWS (dashed line). Right: comparison between the local density $\Sigma_{0.5\,\mathrm{Mpc}}$ adopted in this work, which is the number density within a projected distance of 0.5 Mpc, and $\Sigma_{1.0\,\mathrm{Mpc}}$ within a projected distance of 1.0 Mpc (upper) and $\Sigma_{5\mathrm{th-nearest}}$ within a projected distance to the 5th-nearest neighbor (lower). The neighbors were identified among all members (black solid lines) and massive ($\log M_*/M_\odot > 10$) ones (red dotted lines) within $\Delta v < 1000$ km s^{-1}. The Spearman rank correlation coefficient r_s between local densities is printed in the bottom right of each panel.

(A color version of this figure is available in the online journal.)

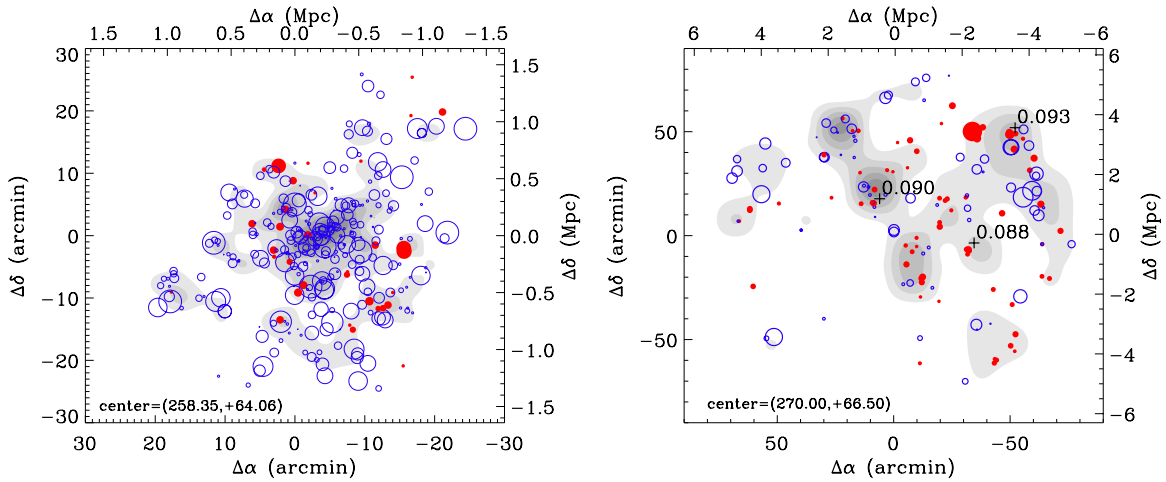

Figure 12. Spatial distribution of galaxies in A2255 (left) and the ANWS (right), on the smoothed galaxy number density map. Red or blue circles represent galaxies with redshifts above or below $z = 0.087$, respectively. The symbol size is proportional to the redshift deviation from the NEP supercluster mean redshift ($z = 0.087$).

(A color version of this figure is available in the online journal.)

include the circumstellar dust emissions. These three models without AGB dust cannot produce the MIR-excess colors of N3 − S11 > −2 of red and early-type galaxies, although the circumstellar dust formation and the evolution of AGB stars are still known to be uncertain in detail. From two model SEDs including AGB dust we can set a threshold in MIR color (N3−S11) to divide galaxies into MIR-red galaxies (N3−S11 > 0) and MIR-blue galaxies (N3−S11 < 0). Also, N3−S11 > −1 divides relatively young (2–5 Gyr old) passive ellipticals and old ellipticals. In summary, the MIR-red galaxies are dominated by SF, late types in our sample because of little contamination by AGNs, while most of the MIR-blue galaxies are early types showing a wide range of MIR-weighted mean stellar ages.

Figure 15 shows the N3−S11 color versus SSFR derived from the SED fits. This reveals that the N3 − S11 color correlates well with SSFR, indicating that the N3 − S11 color probes different levels of SFA. Specifically, we find that our MIR color cut (N3 − S11 = 0) is comparable to log (SSFR) ∼ −10.7, i.e., galaxies with log (SSFR) < −10.7 (which corresponds to an SFR of 0.2 $M_\odot$ yr^{-1} at a stellar mass of $10^{10}\,M_\odot$) can be considered as passively evolving galaxies. This SSFR cut was adopted by Gallazzi et al. (2009) to separate SF galaxies from quiescent ones. However, in the case of MIR-blue galaxies, the derived SSFR may not have any physical significance as a measure of the current SFA, but may indicate a wide dispersion of mean stellar ages among those passive galaxies if the P03 model SEDs are adopted.

Now we further divide optically red galaxies into four classes depending on their N3 − S11 colors. We made the morphological classification of galaxies in the ANWS field sample using the CFHT r'-band images of 0.″187 pixel^{-1}: early types are bulge dominated with good symmetry (0 and 1 in Figures 16–20), while late types are disk dominated with asymmetric internal structure (2, 3, and 4 in Figures 16–20). The dominant morphological type and its fraction are shown in Table 4.

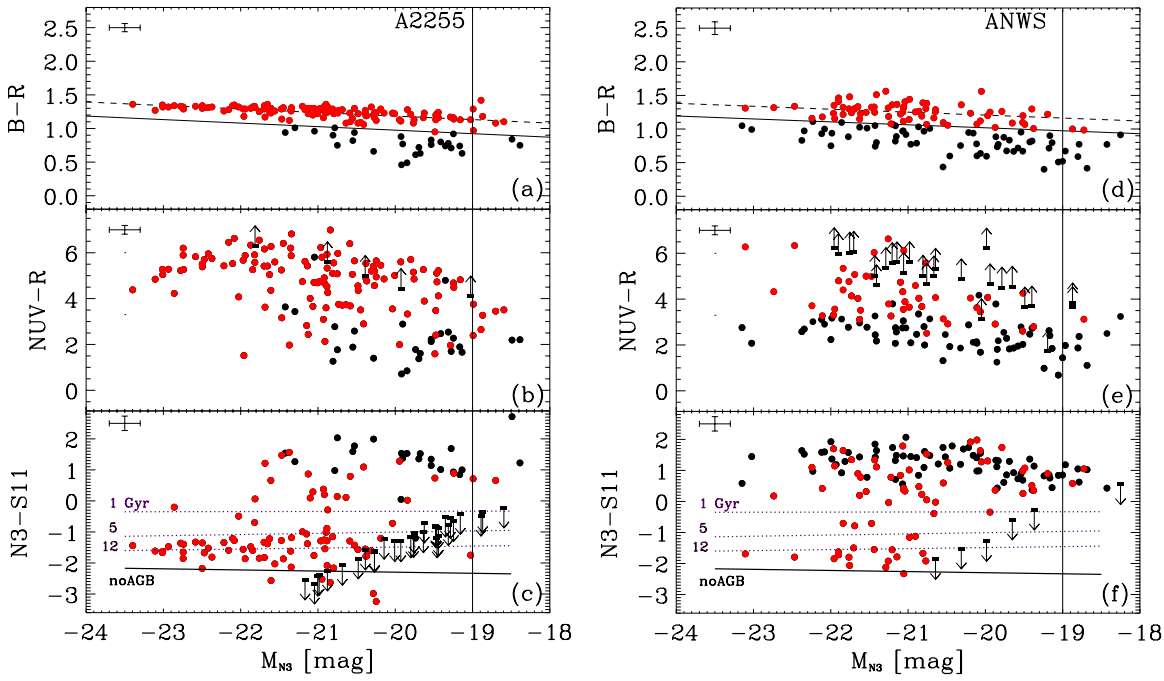

Figure 13. Top: the $B-R$ vs. absolute N3 color–magnitude (CM) diagram for galaxies brighter than $M_{N3}=-19$ in A2255 (left) and in the ANWS (right). The CMR is shown by the dashed line and the horizontal solid line indicates the color cut adopted to classify red galaxies (redward of the solid line). The CMR in the ANWS is normalized to the red sequence of A2255. The color deviation from the CMR is defined as $\Delta(B-R)=0.21(\sim 3\sigma)$, where σ is the standard deviation of residuals to CMR fit. The cross in the upper left corner indicates the typical errors. Middle: the NUV $-$ R vs. absolute N3 CM diagram for galaxies in A2255 (left) and in the ANWS (right). The *GALEX* Nearby Galaxy Survey NUV detection limits are shown for undetected galaxies (arrows). Bottom: the N3 $-$ S11 vs. absolute N3 CM diagram for galaxies in A2255 (left) and in the ANWS (right). The dotted lines indicate the CMR calculated from the P03 AGB model SSPs, assuming a metallicity sequence at three different stellar ages (1, 5, and 12 Gyr, respectively). The horizontal solid line represents the P03 model SSPs without AGB dust. The *AKARI* S11 detection limits are given for undetected samples in S11 (arrows). The vertical line indicates the magnitude cut (N3 $\approx$ 19 corresponding to $M_{N3}=-19$ at the distance of the NEP supercluster).

(A color version of this figure is available in the online journal.)

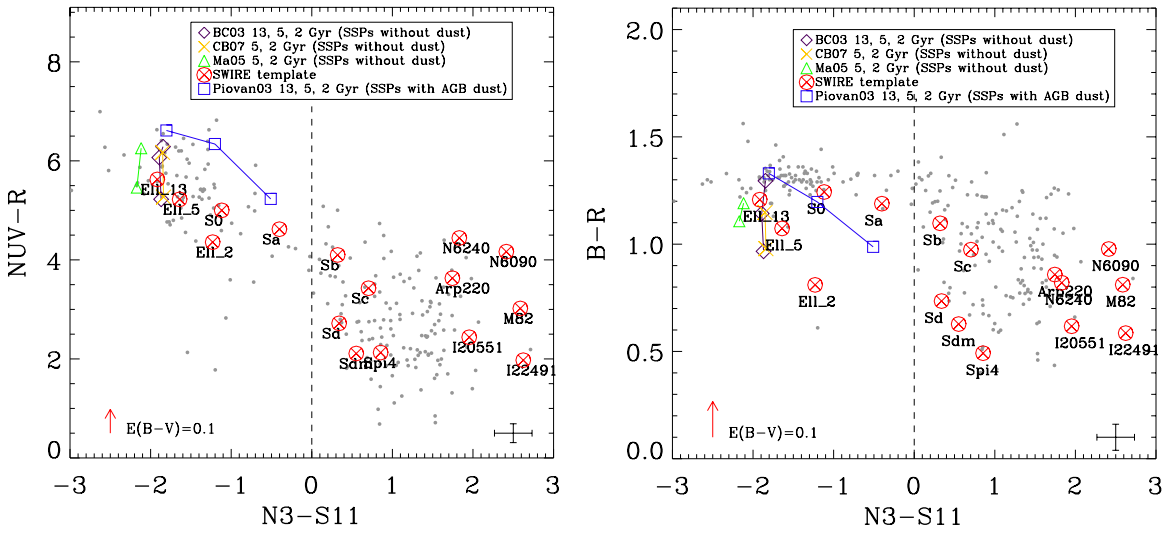

Figure 14. Rest-frame N3 $-$ S11 vs. NUV $-$ R (left) and N3 $-$ S11 vs. $B-R$ (right) color–color distribution of galaxies detected in all four bands, compared with SWIRE templates of Polletta et al. (2007) including three ellipticals (2, 5, 13 Gyr), seven spirals (S0, Sa, Sb, Sc, Sd, Sdm, Spi4), and six starbursts (M82, Arp220, N6090, N6240, I20551, I22491). Also plotted are SSP templates from different libraries (BC03, CB07, Ma05, and Piovan03) with a Salpeter (1955) IMF and a solar metallicity ($Z=0.02$) for the same ages as SWIRE ellipticals. Templates with N3 $-$ S11 >0 are spirals or starbursts, while early types have N3 $-$ S11 <0. The arrow shows the mean value of a reddening vector of $E(B-V)=0.1$ using the Calzetti et al. (2000) extinction law, and the cross in the bottom right corner indicates the typical errors.

(A color version of this figure is available in the online journal.)

First, we classify optically red galaxies with N3 $-$ S11 <-1 (weak MIR-excess galaxies, hereafter weak-MXGs). The SEDs of these galaxies indicate that they have passively evolving, old stellar populations with a mean stellar age greater than 2–5 Gyr. We note that the absolute age should not be taken too seriously considering that the mean stellar ages for a given N3 $-$ S11 color vary depending on the model used. They may have a small amount of MIR excess at 11 μm, but that can be well

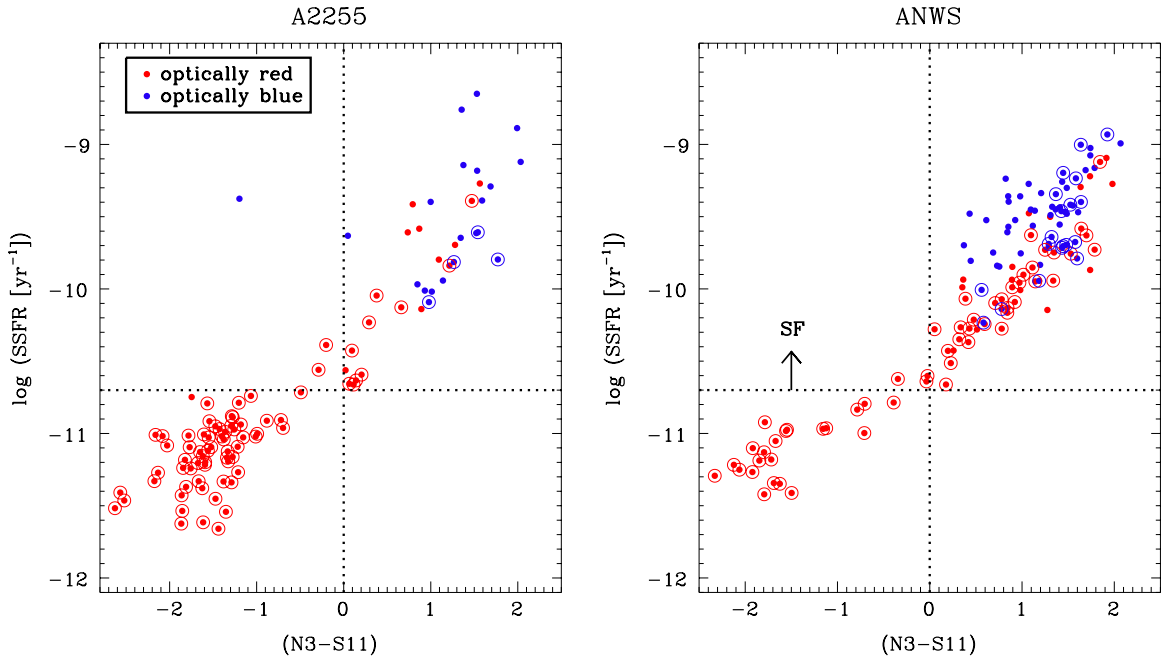

Figure 15. SSFRs derived from the SED fits and N3 − S11 colors of galaxies detected in the N3 and S11 bands. The filled red and blue circles are optically red and blue galaxies classified by the optical CMR (Figure 13). The open circle indicates massive galaxies (log $M_*/M_\odot > 10$). The vertical and horizontal dotted lines indicate our NIR − MIR color (N3 − S11 = 0) and SSFR (log(SSFR) = −10.7) cuts, respectively, that were adopted to separate SF galaxies from quiescent ones following Gallazzi et al. (2009).

(A color version of this figure is available in the online journal.)

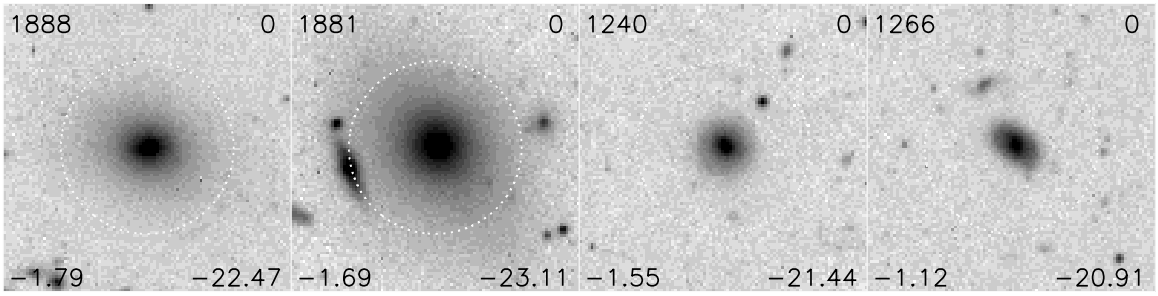

Figure 16. Optical (CFHT r' band) images (60″ × 60″) of the most massive galaxies with optically red and N3 − S11 < −1 (weak-MXGs). Each image lists the object Id, morphology, absolute N3 magnitude, and N3 − S11 color, on the top left, top right, bottom right, and bottom left, respectively. The morphology is classified by eye: 0, bulge dominated; 1, bulge dominated with disk feature; 2, disk dominated with symmetric spiral; 3, disk dominated with asymmetric spiral, and 4, others (merging system or unclassified).

Table 4
Galaxy Classification

Galaxy Type (1)	Optical Color (2)	IR Color (3)	log(SSFR (yr^{-1})) (4)	Morphology Fraction (5)	Comments
Weak-MXG	Red	N3 − S11 < −1	−11.2	Early type (>90%)	Passively evolving galaxies
Intermediate-MXG	Red	−1 < N3 − S11 < 0	−10.8	Early type (>71%)	Transition populations
Weak-SFG	Red	N3 − S11 > 0	−10.3 (−10.7 ∼ −10.0)	Late type (>67%)	Transition populations
Dusty-SFG	Red	N3 − S11 > 0	−9.7 (−10.0 ∼ −9.0)	Late type (>88%)	SF galaxies
Blue-SFG	Blue	N3 − S11> 0	−9.5 (−10.2 ∼ −8.9)	Late type (>93%)	SF galaxies

Notes. Column 1: classified galaxy type; Column 2: first, the optical color–magnitude relation (CMR) is used to separate *red* from *blue* galaxies; Column 3: second, the *red* galaxies are subdivided by NIR−MIR (N3 − S11) color; Column 4: the mean values of specific star formation rate (SSFR) in units of dex. For SF populations, the range of SSFR is enclosed in brackets; Column 5: the dominant morphology from visual classification, and the fractions of early types: 0, 1 and late types: 2, 3, 4 (see the caption in Figure 16).

understood within the framework of passively evolving galaxies with AGB dust. Figure 16 shows the CFHT r'-band images of these galaxies. As the figure shows, their morphologies are predominately early type. Therefore, these are passively evolving early-type galaxies.

The second class comprises optically red galaxies with −1 < N3 − S11 < 0 (intermediate MIR-excess galaxies, hereafter intermediate-MXGs). The SEDs suggest that they are either relatively young (compared to the weak-MXGs), passively evolving galaxies (⩽2–5 Gyr) or very weakly SF galaxies

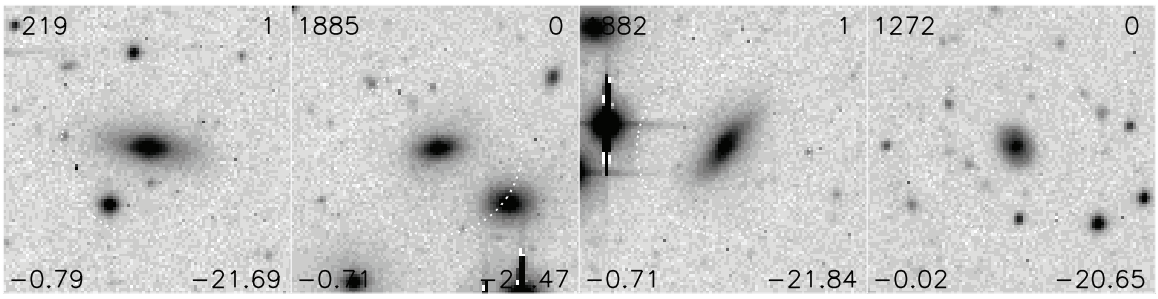

Figure 17. Same as Figure 16, but for the galaxies with optically red colors and $0 < \mathrm{N3} - \mathrm{S11} < -1$ (intermediate-MXGs).

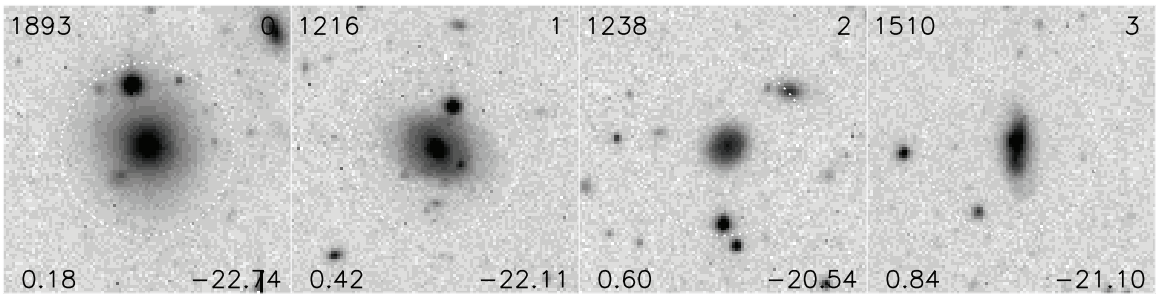

Figure 18. Same as Figure 16, but for the galaxies with optically red colors and $\mathrm{N3} - \mathrm{S11} > 0$ (log SSFR < -10; weak-SFGs).

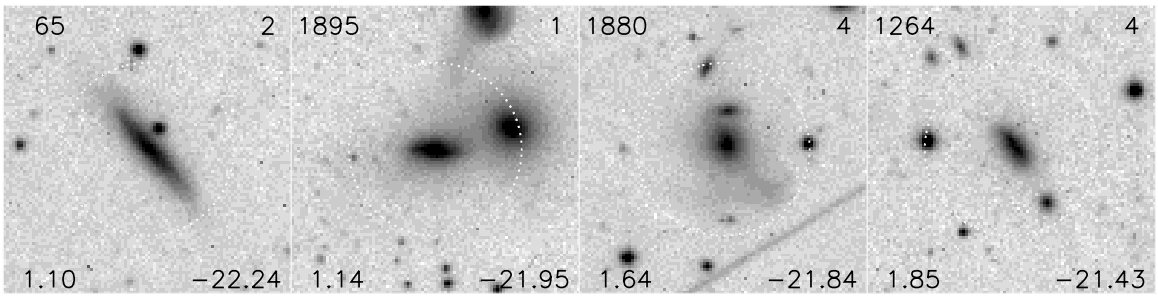

Figure 19. Same as Figure 16, but for the galaxies with optically red colors and $\mathrm{N3} - \mathrm{S11} > 0$ (log SSFR > -10; dusty-SFGs).

(around 36% of them have log(SSFR) > -10.7, but are very near the cut in Figure 15). If left alone, they are most likely to evolve into old, passively evolving galaxies. Figure 17 shows sample images of these galaxies, which are mostly early types (i.e., 71% of the ANWS intermediate-MXGs are early types).

The optically red galaxies with $\mathrm{N3} - \mathrm{S11} > 0$ (strong MIR-excess galaxies, hereafter strong-MXGs) consist of weak SF galaxies with log(SSFR) < -10 (∼45%, hereafter weak-SFGs) and dusty SF galaxies with log(SSFR) > -10 (∼55%, hereafter dusty-SFGs). Interestingly, the mean value of log(SSFR) for dusty-SFG is comparable to that of blue SF galaxies (hereafter blue-SFGs) with log(SSFR) of −9.7 versus −9.5 and higher than weak-SFG of −10.3. Both blue-SFG and dusty-SFG are thus vigorously SF galaxies. They may eventually stop star formation and evolve into the earlier types. Figures 18 and 19 show the r'-band images of weak-SFG and dusty-SFG, respectively, which suggest that they have disk-like morphology. Interestingly, more than half of dusty-SFGs are edge-on disks, indicating that half of these are viewed at higher disk inclination. Thus, we can speculate that the dusty-SFGs are strong SF late-type galaxies, but optically reddened. On the other hand, weak-SFGs have relatively lower SSFR than the blue-SFGs, thus we can expect that their current/recent star formation is insufficient to change their optical color. In other words, in the weak-SFGs, the dominant stellar populations are generally old (no hot young stars, i.e., the average stellar age is greater than 1 Gyr) although their MIR-red colors ($\mathrm{N3} - \mathrm{S11} > 0$) indicate that they have recently formed some stars (<1 Gyr traced by P03 model) and/or have a low level of ongoing star formation. Moreover, their dominant disk-like morphology (i.e., spirals) also indicates that a significant SFA could not have stopped very long ago, because spiral features fade within a few Gyr without an interstellar gas supply (Lin & Shu 1964; Bekki et al. 2002; Masters et al. 2010). It is therefore possible to conclude that, in terms of morphological transformation, weak-SFGs are precursors of the second class (intermediate-MXG). This is supported by the recent result of Hopkins et al. (2009) who suggest that disk galaxies with small gas fractions are more likely to be transformed into spheroids through minor mergers.

Our classification scheme in four different populations based on the MIR color is summarized in Table 4. However, dusty-SFG could be an edge-on subsample of the blue SF galaxies because both have similar SSFR, indicating that both populations are at the same evolutionary stage. The only difference is that dusty-SFGs are more likely to be edge-on. Therefore, we divide galaxies into passively evolving population ("weak-MXG"), transition populations ("intermediate-MXG" and "weak-SFG"), and strong SF populations ("dusty-SFG" and "blue-SFG").

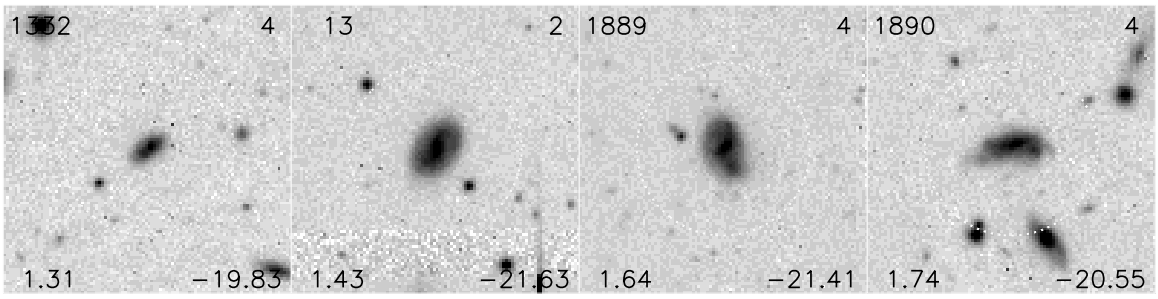

Figure 20. Same as Figure 16, but for the galaxies with optically blue colors and N3 − S11 > 0 (blue-SFGs).

4.3. Transition Populations

4.3.1. Weak SF Galaxies (Weak-SFGs)

The weak-SFGs in our sample show low levels of SFA (on average ∼4 times smaller SFRs than the blue-SFG at the fixed mass range log $M_*/M_\odot = [9.5, 11]$). However, their optical red colors are mostly due to their underlying old stellar populations, and not an effect of dust reddening. In other words, they have older stellar populations and smaller SFRs (insufficient to change the optical color) compared to blue-SFG. Furthermore, they have mostly disk-dominated morphologies. Therefore, in terms of SFA in galaxy evolution, our weak-SFGs are possible candidates for the transition population in which star formation is suppressed, compared to blue-SFG, and their red colors are due to old stellar populations. These populations are very similar to "anemic spirals" discovered by van den Bergh (1976), which are thought to be in the transition from blue, SF field spirals to red, non-SF cluster S0 galaxies. They are also generally at a similar evolutionary stage to the transition populations (red spirals or red SFs) selected using different criteria in other works using SDSS galaxies (e.g., Bamford et al. 2009; Masters et al. 2010) and galaxies in the Abell 901/902 supercluster at redshift ∼0.17 (e.g., Gallazzi et al. 2009; Wolf et al. 2009).

4.3.2. Intermediate MIR-excess Galaxies (Intermediate-MXGs)

The intermediate-MXGs in our sample are defined as bluer in N3 − S11 colors (indicating lower SSFRs) than weak-SFG, but redder (indicating younger ages) than weak-MXG. This implies that their MIR emission arises from very weak SFA (on average ∼3.2 times lower SFR than weak-SFG) or AGB stars with intermediate ages of 1–5 Gyr (i.e., past SFA). However, their optical red colors are definitely from an old stellar population, because their estimated mean value of E_{B-V} (∼0.05) is similar to weak-MXG. Although the origin of the MIR emission is complex, the mean stellar ages of intermediate-MXG traced by the amount of warm dust emission per stellar mass are obviously older than the ages of the weak-SFG and younger than the weak-MXG. Thus, it is possible that this population is on the evolutionary stage of migration to weak-MXG from weak-SFG, or directly from blue-SFG. Furthermore, in contrast to weak-SFG, the dominant morphologies of intermediate-MXG are early types (more than 71%), supporting the idea that these are in the final transition phase just before passively becoming weak-MXG. Therefore, our intermediate-MXGs represent populations where major SFA ended over 1 Gyr ago. The MIR-weighted mean stellar ages for these galaxies are 1–5 Gyr, if we assume single-burst stellar populations. This result can be explained if the MIR-excess emission of red, early-type galaxies is mainly from AGB stars (Ko et al. 2009). It is supported by Vega et al. (2010), who suggest that the unusual PAH emission in the 6–14 μm region in nearby early-type galaxies arises from intermediate-age carbon stars, and they can be formed by rejuvenation episodes within the last few Gyr at the 1% level of the mass of the galaxy.

Our intermediate-MXGs seem to be closely related to the UV-excess galaxies in Yi et al. (2005). They found that roughly 15% of nearby early-type galaxies have excess NUV emission indicating recent (<1 Gyr) star formation comprising 1%–2% of the total stellar mass. Around 1 Gyr after a single burst of star formation, massive stars (O, B, and A stars) have expired, and recent star formation indicators (e.g., NUV flux and Hβ line index) are no longer good tracers of the star formation history. However, the MIR-excess emission over stellar light can trace star formation over a much longer period, since low- to intermediate-mass (1–9 $M_\odot$) stars evolve to the AGB phase and their circumstellar dust emission is strong in the MIR. Frogel et al. (1990) found that the contribution of AGB stars to the bolometric luminosity peaks at more than 40% at ages from 1.1 to 3.3 Gyr, but rapidly falls to less than 5% at 10 Gyr. In other words, our intermediate-MXGs seem to be a population of descendants of objects showing recent SFA within ∼1 Gyr, which are UV-excess early-type galaxies and post-starburst (E+A) galaxies (Choi et al. 2009a). However, we expect that those young early-type galaxies have different evolutionary histories from our weak-SFG due to their different morphologies.

5. ENVIRONMENTAL AND MASS DEPENDENCE OF GALAXIES IN TRANSITION PHASE

We now investigate how the properties of galaxies are influenced by their stellar mass and local environment. We focus on the intermediate-MXG and the weak-SFG as objects that might be in the evolutionary transition from blue, SF late types to red, passive early types.

If the properties of galaxies are affected by environmental mechanisms, such as hydrodynamic or gravitational processes (e.g., Boselli & Gavazzi 2006 and Park & Hwang 2009 for a review), we expect to see an increase of transition populations in specific environments. For example, when blue spiral galaxies infall from low- to high-density regions (although it depends on the relevant timescale), both global halo properties and/or the local galaxy density can produce a gradual/sharp decline of star formation and morphological transformation by external factors, such as tidal interactions and gas stripping. As a result, SF galaxies in dense regions show lower SFR, and the fraction of early-type galaxies increases with increasing density or toward the center of the galaxy cluster.

On the other hand, if the effects of stellar mass on the galaxy properties are stronger than those of environment, then we would not expect any significant changes in the distribution of transition galaxies over a range of local density at fixed

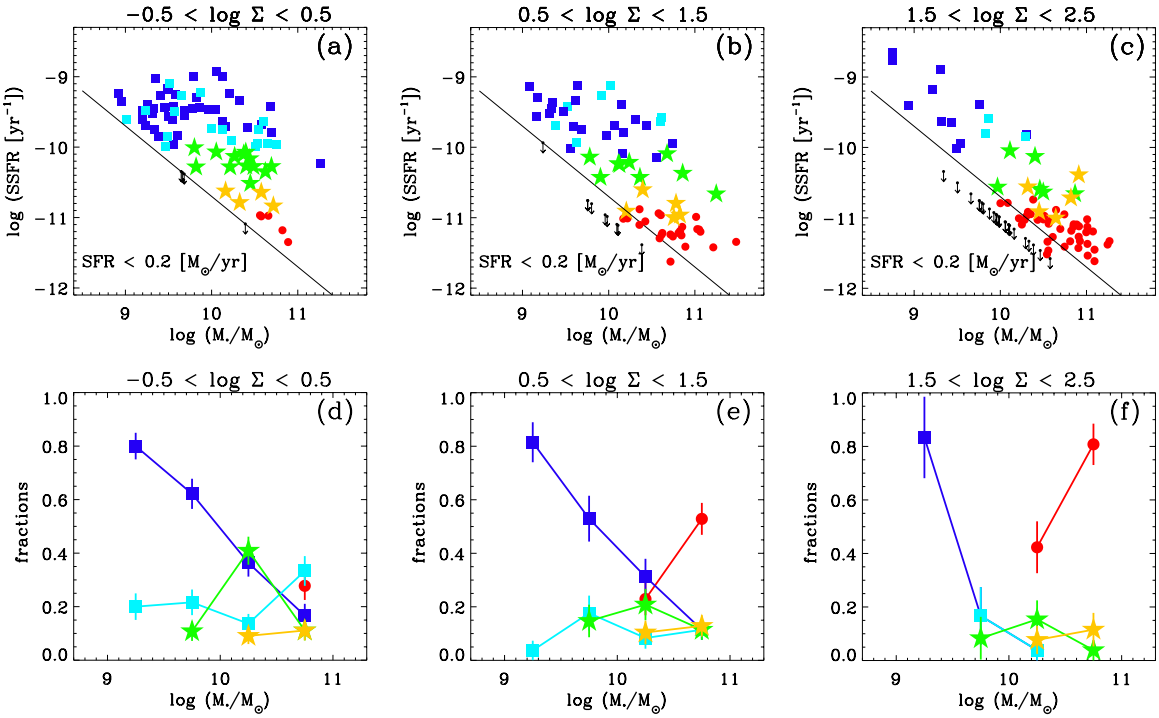

Figure 21. Upper: SSFR as a function of stellar mass in three density bins for our N3-selected supercluster member galaxies in A2255 and in the ANWS. Local density is increasing from left to right. The red circle, yellow star, green star, cyan square, and blue square represent weak-MXG, intermediate-MXG, weak-SFG, dusty-SFG, and blue-SFG, respectively. Circles, stars, and squares also represent passively evolving, transition, and strong SF populations, respectively. The small circle with an arrow represents the object that is undetected in S11 (see Figure 13), and the solid lines in each panel show the detection limit of 0.2 $M_\odot$ yr^{-1} for the ANWS sample. Lower: the fraction of each galaxy type as a function of stellar mass. Type fractions are defined as the ratio between the number of galaxies in each type class and the total number of galaxies at a fixed mass. The errors are calculated assuming that the fractions are the maximum values of the likelihood function (see the text for details). The total number of galaxies includes objects that are undetected in S11. Mass bins with less than three galaxies are excluded.

(A color version of this figure is available in the online journal.)

stellar masses. In this case, the stellar mass is the primary parameter governing the suppression of star formation and the transformation of morphology, and thus transition populations would only show a trend with their stellar mass.

In an attempt to analyze the dependence of the properties on the stellar mass and the environment independently, we plot the change in the relative fraction of different types of galaxies as a function of the stellar mass at low-, intermediate-, and high-density regions (Figure 21), and as a function of the local density at different mass bins (Figure 22). Here, Σ is used for the local density, as described in Section 3.2. The type fraction (f_t) is defined as the ratio of the number of each galaxy type (N_t) to the total number of galaxies ($N_{\rm total}$) in fixed mass and density bins. We include S11-undetected samples to calculate $N_{\rm total}$. The uncertainties of the fractions are estimated by calculating the variance in the likelihood of the fraction (e.g., De Propris et al. 2004). Assuming that the fraction has the form of the likelihood function

$$L \propto f_t^{N_t}(1-f_t)^{N_{\rm total}}$$

and its maximum is $N_t/N_{\rm total}$, the variance of the fraction is

$$\sigma^2(f_t) = \left(\frac{d^2 \ln L}{df_t^2}\right)^{-1},$$

when the likelihood function has a Gaussian form. Note that our estimate of the standard deviation might be low due to the distribution of our small samples (i.e., the likelihood function may not be Gaussian). In order to avoid the lower detection rate of galaxies with N3 − S11 < 0 (only the weak-MXG and intermediate-MXG are contained in our N3-selected sample) due to the S11 detection limit, Figure 23 shows galaxies at stellar mass bin log $M_*/M_\odot$ = [10, 11]. We include S11-undetected samples as part of the weak-MXG since their SSFRs are low enough. Table 5 summarizes the results in Figure 23. From Figures 21−23 and Table 5, our results can be summarized as follows.

1. We find that the weak-SFGs are mostly dominant at mass bin log $M_*/M_\odot$ = [10, 10.5] and at density bin log Σ = [−0.5, 0.5] (Figures 21(d) and 22(e)). In this mass range (Figure 22(e)), more than 20% of the population in all density bins are the weak-SFGs, and, in particular, the weak-SFGs are the dominant population in the density bin of log Σ = [−0.5, 0.5] (∼40%). Interestingly, this density bin corresponds to the region in the outskirts of A2255 and the intermediate-density regions of the ANWS. This is confirmed in Figure 24, which shows the distribution of each galaxy type only for the most massive galaxies (log $M_*/M_\odot$ > 10) on the number density maps of all member galaxies. The weak-SFGs tend to avoid the central region of A2255 (the two weak-SFGs close to the center have redshifts of 0.07379 and 0.07387, placing them at the edge of the velocity distribution of A2255, so that their location is likely a projection effect). However, when galaxies in both more-massive (log $M_*/M_\odot$ = [10.5, 11.0]; Figure 22(f)) and less-massive (log $M_*/M_\odot$ = [9.5, 10.0]; Figure 22(d)) bins are considered, the weak-SFGs are not as significant, contributing with less than

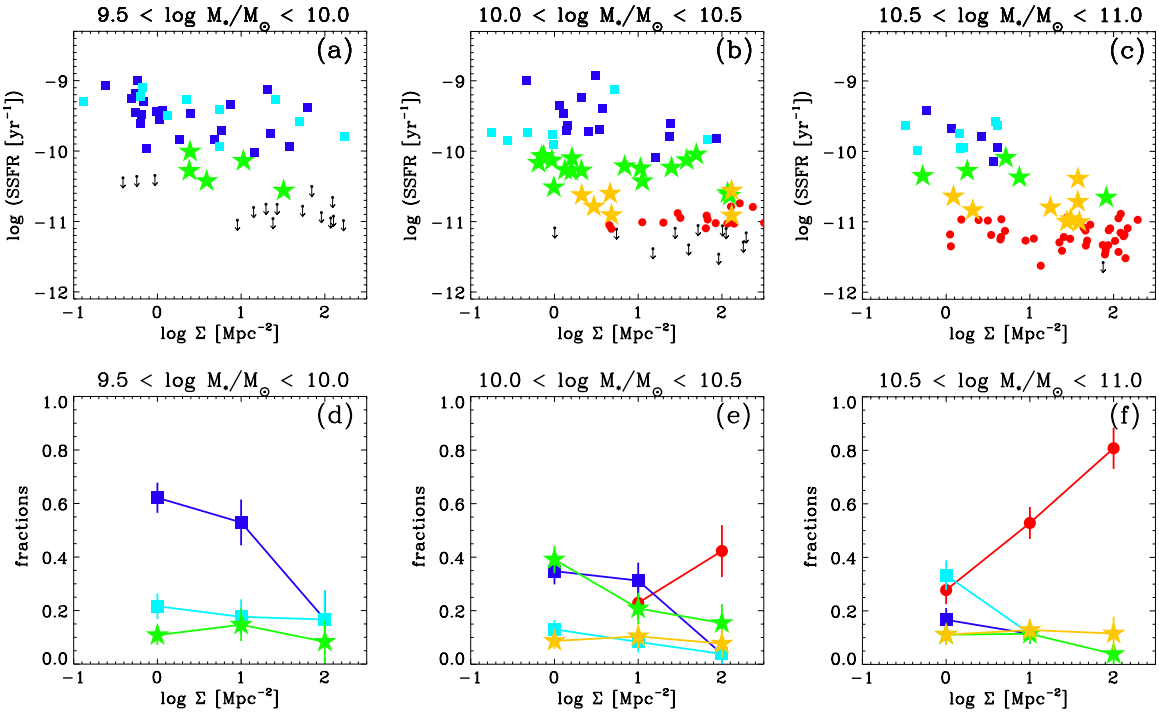

Figure 22. Upper: SSFR as a function of galaxy local density in three stellar mass bins for our N3-selected supercluster member galaxies in A2255 and in the ANWS. The symbols are the same as in Figure 21. Lower: the fraction of each galaxy type as a function of local density.

(A color version of this figure is available in the online journal.)

Table 5
The Fraction of Each Galaxy-type in Figure 23(c).

Galaxy Type	$\log M_*/M_\odot = [10, 11]$		
	Low Density (%) ($-0.5 < \log \Sigma < 0.5$)	Intermediate Density (%) ($0.5 < \log \Sigma < 1.5$)	High Density (%) ($1.5 < \log \Sigma < 2.5$)
Weak-MXG	14	43	76
Intermediate-MXG	10	12	10
Weak-SFG	27	15	10
Dusty-SFG	22	10	2
Blue-SFG	27	20	2

20% of the population in any density bins, and their environmental trend is weaker. Note that, although the weak- and intermediate-MXGs are not detected in the lowest mass bin because of the S11 detection limit, our result matches well the trend of red spirals of Wolf et al. (2009; see their Figure 15).

2. At log $M_*/M_\odot > 10$, the overall fraction of SF galaxies (blue-, dusty-, and weak-SFGs) decreases gradually by ∼76%, ∼45%, and ∼14% in low-, intermediate-, and high-density bins, respectively (see Figure 23(c)). The overall fraction of red galaxies increases increasing local density (see Figure 23(d)). This is basically a confirmation of the SFR–density relation (e.g., Lewis et al. 2002; Kauffmann et al. 2004; Weinmann et al. 2006; Hwang et al. 2010) and CDR (e.g., Pimbblet et al. 2002; Blanton et al. 2005; Cucciati et al. 2006). This trend indicates that massive galaxies are mostly red in all environments and comprise most of the galaxies in the highest density regions. However, if optically red galaxies are divided into four different sub-populations, then the interpretation needs to be done carefully. If we focus on the weak-MXG (Figure 23(c)), there is a strong environmental dependence, there being a very small fraction of weak-MXGs in the lowest density bin. However, the fraction of red galaxies presents a high value (∼73%, see Figure 23(d)) in the lowest density bin due to the rather high proportion of SF galaxies (weak- and dusty-SFGs) that are red.
3. The relative fraction of weak-SFGs among SF galaxies (weak-, dusty-, and blue-SFGs), as a function of local density at fixed mass, allows us to study the importance of mass/environment in SF quenching. In Figure 25(a), at all local densities, the relative weak-SFG fraction is higher at large stellar mass (log $M_*/M_\odot > 10$) than at low stellar mass (log $M_*/M_\odot < 10$). The fraction of weak-SFGs is ∼ twice as high at the highest density bin, compared with the lowest density bin when only massive galaxies are considered. However, for less massive galaxies, the fraction does not change significantly with the local density. This suggests that the weak-SFGs are likely to be more massive than strong SF galaxies (dusty- and blue-SFGs) and comprise a significant fraction of all massive SF galaxies in high-density environments.
4. We find roughly 10% intermediate-MXGs among all massive (log $M_*/M_\odot > 10$; Figure 23(c)) galaxies in

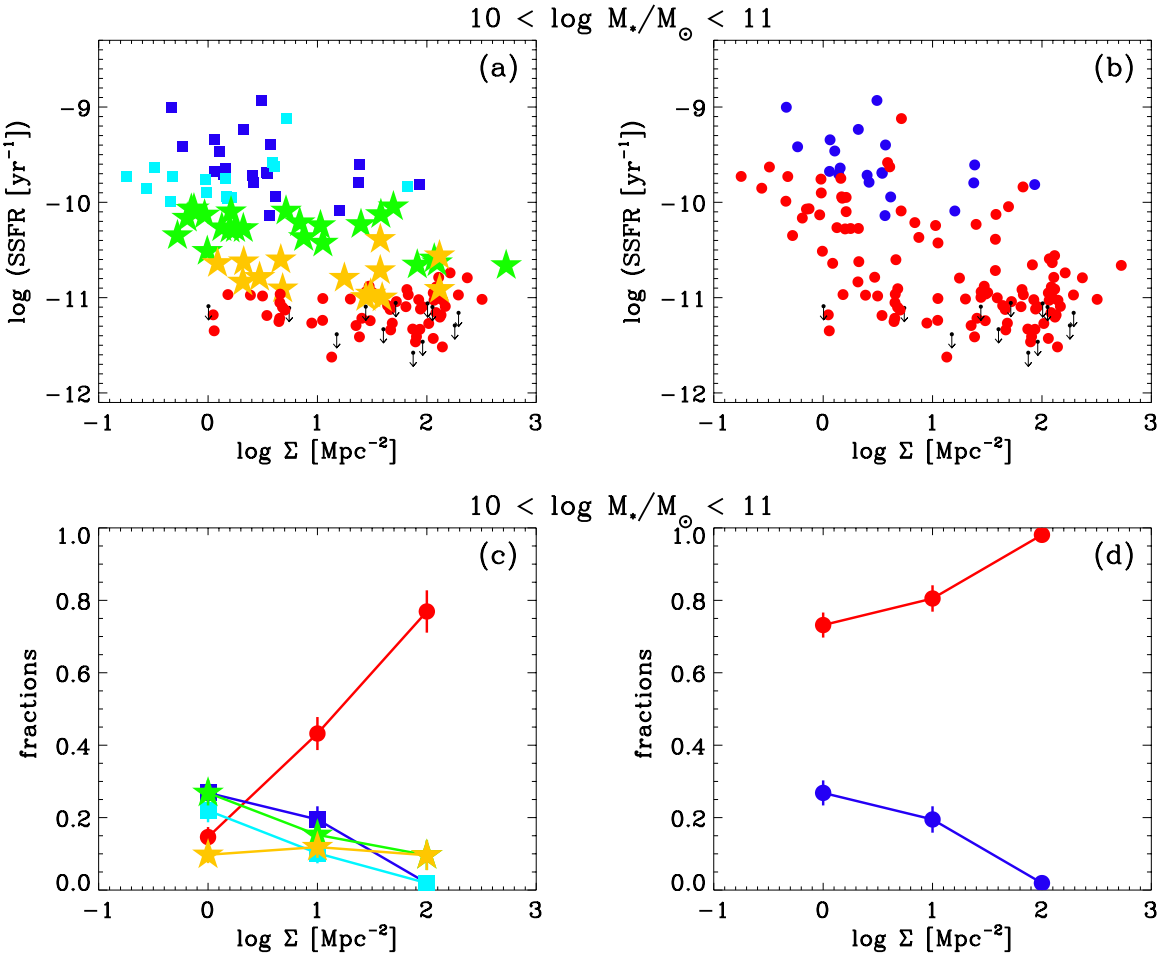

Figure 23. Upper: SSFR as a function of galaxy local density at stellar mass bin log $M_*/M_\odot = [10, 11]$ for our N3-selected supercluster member galaxies in A2255 and in the ANWS. In the left panel, each galaxy type is the same as in Figure 21, while red and blue circles in the right panel indicate optical red and blue galaxies which are divided using the $B - R$ vs. M_{N3} CMR (see Figure 13 for details). Lower: the fraction of each galaxy type as a function of local density. Undetected samples in S11 are counted as the weak-MXGs (left) and red (right) due to their low SSFRs.

(A color version of this figure is available in the online journal.)

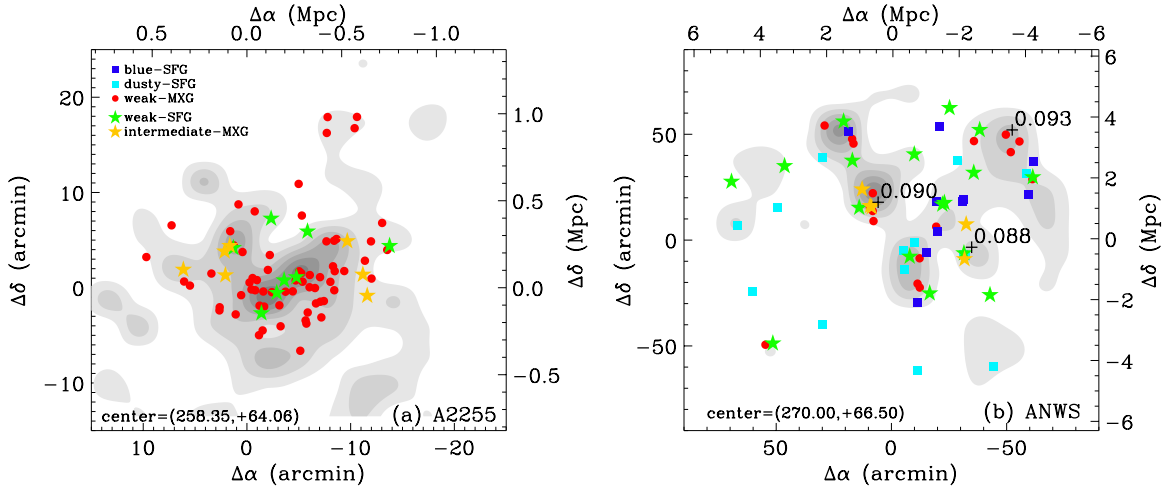

Figure 24. Spatial distribution of each galaxy type in Figure 23, on the smoothed galaxy number density maps for all supercluster member galaxies in A2255 (left) and in the ANWS (right). In the right panel, the three "+" signs indicate the center of X-ray detected groups with the mean redshifts given (Henry et al. 2006). North is up and east is to the left.

(A color version of this figure is available in the online journal.)

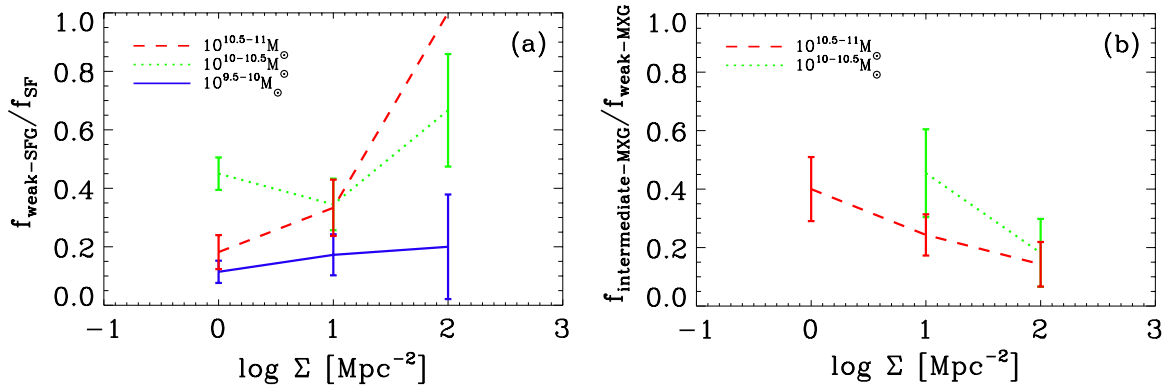

Figure 25. Left: the fraction of weak-SFG among SF galaxies (weak-, dusty-, and blue-SFGs) is plotted as a function of local density in three stellar mass bins: log $M_*/M_\odot$ = [9.5, 10], [10, 10.5], and [10.5, 11]. Right: the relative fraction of the intermediate-MXG vs. the weak-MXG is plotted as a function of local density in two stellar mass bins: log $M_*/M_\odot$ = [10, 10.5] and [10.5, 11]. Because of the cut in S11, less-massive (log $M_*/M_\odot < 10$) MIR-blue (N3 − S11 < 0) galaxies are not detected.

(A color version of this figure is available in the online journal.)

all density bins. However, the relative fraction of these versus the weak-MXG decreases as the density increases by ∼42%, ∼22%, and ∼12%, respectively. Thus, about half of the massive early-type galaxies on the red sequence at the outskirts of the cluster show significant excess MIR emission compared to normal (passively evolving) early-type galaxies. In Figure 25(b), when the intermediate-MXGs are divided into two mass bins (log $M_*/M_\odot$ = [10, 10.5], [10.5, 11]), the relative fraction of the intermediate-MXG is higher in the lower-mass bin. It is thus possible to infer that the intermediate-MXGs are less massive and tend to be located in the outer parts of the cluster. This is largely consistent with our study of the galaxies in A2218 (Ko et al. 2009). Although the size of our mass-limited sample of intermediate-MXG is too small to determine the mass dependence for this population, we can see the environmental dependence for massive galaxies. In Figure 24, the intermediate-MXGs are likely to be located in the outskirts of the cluster and near group centers (corresponding to the lowest density bin in Figure 25(b)). Therefore, an environmental action is necessarily required to explain the properties of this population. It is expected that the intermediate-MXGs evolve into weak-MXGs. Furthermore, SSFRs (approximately MIR-weighted mean stellar ages) of the intermediate-MXGs are much smaller than those of weak-SFGs, indicating that the weak-SFGs are at an earlier evolutionary stage than the intermediate-MXGs. Also, the main difference between both transition populations is the morphology (disk-dominated for weak-SFG and bulge-dominated for intermediate-MXG).

6. DISCUSSION

Recent studies of red galaxies defined by optical CMR cuts indicate that they contain several populations at different evolutionary stages (e.g., Lee et al. 2008; Ko et al. 2009; Cortese & Hughes 2009; Wolf et al. 2009; Gallazzi et al. 2009; Tran et al. 2009; Bamford et al. 2009; Bundy et al. 2010; Masters et al. 2010; Salim & Rich 2010). For example, red, early-type galaxies are found to have a wide range of MIR excess of non-stellar origin, suggesting that some of these experienced recent star formation episodes. In addition, some red-sequence galaxies are found to have UV excess suggesting weak SFA.

We expect that there are two different phases (star formation quenching and morphology changing), when a blue, SF, late-type galaxy turns into a red, quiescent, early-type galaxy. Recent studies revealed that star formation quenching (optical color change) is not always accompanied by morphological change (e.g., Blanton et al. 2005; Sánchez et al. 2007; Bamford et al. 2009; Wolf et al. 2009). In other words, the timescale of transition from blue to red and of morphological change from late type to early type is different, and seems to be a function of stellar mass and local galaxy density. Observationally, the existence of red spirals (i.e., weak-SFGs) and blue early-type galaxies, and their preference for specific masses and local densities support this idea.

To trace mass and environment dependence of changes in color and morphology, we focused on two different categories of transition galaxies (intermediate-MXG and weak-SFG). Specifically, their NIR–MIR color (N3−S11) is a good tracer of SSFR, and the SSFR of SF galaxies is not sensitive to their mass and environment (e.g., Peng et al. 2010).

6.1. Transition Populations I: Weak-SFG

Our result that the weak-SFGs are mainly dominant at intermediate mass (log $M_*/M_\odot$ = [10, 10.5]) in the cluster outskirts agrees with previous studies: both Wolf et al. (2009) and Masters et al. (2010) show that red spirals are predominant at intermediate local density (infall regions of clusters) and at the higher mass end ($>10^{10}$ $M_\odot$). Quantitatively, we find that the fraction of weak-SFGs among SF galaxies (blue-, dusty-, and weak-SFGs) ranges from 71% at the cluster core to 36% in the outskirts of the cluster, at log $M_*/M_\odot$ = [10, 11]. This suggests that the suppression of star formation progresses rapidly in high-density environments, so that the weak-SFG shifted into quiescence earlier than those in the lower density environments, at a fixed mass ($>10^{10}$ $M_\odot$). This suggests the acceleration of "downsizing" in overdense regions (e.g., Bundy et al. 2006). If we assume the "downsizing" scenario, then galaxies with the same mass and SSFR should have similar star formation histories. However, the much higher weak-SFG fraction among SF galaxies and much lower weak-SFG fraction among red galaxies in high-density environments compared to low-density environments suggest that the star formation of their progenitor galaxies (blue-SFGs) could be suppressed efficiently because of the high galaxy number density and/or much longer interaction

with the cluster environment. Thus, massive weak-SFG in high-density regions could be already replaced by intermediate-MXG and/or weak-MXG.

In contrast, at the highest masses ($\log M_*/M_\odot = [10.5, 11]$), the fraction of weak-SFG is more than two times smaller than the mass cut ($\log M_*/M_\odot < 10.5$) in all density bins (<10% of all galaxies). This can be interpreted as a mass-dependent star formation history where massive galaxies are much older, became passive earlier than less massive galaxies, and have been undergoing a much higher frequency of mergers, so that their morphologies have already transformed to early types.

At lower masses ($\log M_*/M_\odot = [9.5, 10]$), even considering our S11 detection limit, the fraction of weak-SFGs among SF galaxies appears to decrease sharply at all density bins, compared to larger masses (see the left panel of Figure 25). This is consistent with the results of Wolf et al. (2009) where they suggest that the star formation of low-mass galaxies in clusters is suppressed quickly and the morphological change happens simultaneously, hence red spirals are very rare (see also Boselli et al. 2008). Therefore, we confirm the previous results that low-mass blue-SFGs infalling from outskirts of clusters have experienced halo and disk gas stripping via some environmental effects, and almost simultaneously spiral structures have disrupted into early-type morphology, in contrast to higher-mass galaxies whose spiral structures persist much longer. It is supposed that low-mass galaxies with depleted gas disks are susceptible to morphological change through minor merger events (Hopkins et al. 2009). Furthermore, Masters et al. (2010) also found that the fraction of red spirals with smaller masses ($<10^{10}\ M_\odot$) is very low, in contrast to the larger masses.

From the behavior of the weak-SFG, star formation quenching is affected both by the stellar mass and environment. However, the environmental dependence works differently in each mass bin.

6.2. Transition Populations II: Intermediate-MXG

Another proposed transition population is the intermediate-MXG, which has already been classified in our analysis of A2218 and A2255 (Ko et al. 2009; Shim et al. 2011). These galaxies are optically red and have early-type morphologies, but show broad emission in the MIR (e.g., Bressan et al. 2006). These suggest that the MIR-weighted mean stellar ages of these galaxies are younger than those of the weak-MXGs. They also show a wide range of MIR-excess emission, suggesting a variety of star formation histories among red, early-type galaxies.

In the right panel of Figure 25, although we can only explore massive intermediate-MXGs due to our S11 detection limit, we find that these galaxies are relatively low-mass systems among massive ($>10^{10}\ M_\odot$) red, early-type galaxies and are likely to be located in the outer parts of the cluster. This is consistent with the results in A2218.

At larger masses ($>10^{10} M_\odot$), about 51% of the galaxies show quenched or decreased star formation (i.e., weak- and intermediate-MXGs, and weak-SFG) and around 24% have early-type morphology (i.e., weak- and intermediate-MXGs) in the outskirts of clusters; when the cluster core is considered, these proportions increase to 96% and 86%, respectively. Furthermore, with increasing local density, the relative fraction of these transition galaxies versus the weak-MXG decreases sharply, while versus the weak-SFG it increases. These trends can be explained if the morphological transformation starts at the outskirts and the process is mostly completed at high density, and the intermediate-MXGs are a set of products of morphological transition between the weak-SFG and the weak-MXG at all cluster environments. From the behavior of the intermediate-MXG, morphological transformation of galaxies can be explained by the environmental effects.

The behavior of our transition populations (weak-SFG and intermediate-MXG) suggests a possible scenario of evolutionary history of galaxies, from SF, late-type galaxies to non-SF, early-type galaxies. On this issue, based on the findings above, we can speculate that as the gas supply decreases and the SFRs continue to decline, blue-SFG may naturally change to weak-SFG with gas-poor disks, mainly governed by their mass (massive galaxies evolve faster than less-massive ones in optical color change), and that this transition is accelerated in the high-density environment. Then a large fraction of massive weak-SFG proceeds slowly through several environmental processes, particularly starting at the outskirts of clusters, while for less massive galaxies this happens faster. Finally, they transform into the weak-MXG through the intermediate-MXG. Sánchez et al. (2007) suggested a two-step scenario in which star formation is quenched first and morphological transformation follows on longer timescale, from the analysis of A2218. Sánchez-Blázquez et al. (2009) also suggested that the timescale of morphological transformation of the galaxies entering the red sequence is different from that of star formation quenching.

7. SUMMARY AND CONCLUSIONS

We have investigated the MIR properties of optical red-sequence galaxies within a supercluster in the NEP region at redshift ~0.087, using the ANWS (5.4 deg^2) and *AKARI* IR (2–24 μm) observations of A2255, in conjunction with NUV–optical SEDs and optical spectroscopy. *AKARI* 11 μm flux traces not only the amount of recent SFA but also the presence of intermediate-age stellar populations (i.e., past SFA). Therefore, the NIR−MIR (N3 − S11) color can be a good indicator of SSFRs, whereby we can identify dusty SF galaxies (dusty-SFGs) and transition galaxies among red-sequence galaxies.

We find that ~22% of the massive ($>10^{10}\ M_\odot$) red-sequence galaxies are dusty-SFGs in low-density regions. Their SSFRs are comparable to those of blue-SFGs and their environmental trend is similar to SF populations (blue- and weak-SFGs). Thus, their optical red colors are due to dust extinction or/and higher disk inclination.

We also find that red-sequence galaxies, excepting dusty-SFGs, consist not only of passively evolving galaxies but also of weak-SFGs (disk-dominated SF galaxies which have SSFR lower than blue-SFGs) and intermediate-MXGs (bulge-dominated galaxies showing broad non-stellar MIR emission compared to weak-MXGs). These two populations may represent transition galaxies from blue, SF, late-type galaxies evolving into red, quiescent, early-type ones. In this study, we have focused on properties of these transition galaxies, and on how the fraction of transition galaxies depends on the stellar mass and the local density. Our main conclusions are summarized as follows.

1. The weak-SFGs are found to be similar to the red spirals of the Galaxy Zoo (Masters et al. 2010) and optically passive spirals (Wolf et al. 2009) in the A901/2 cluster. Consistent with previous studies, at the same mass range ($\log M_*/M_\odot = [10, 11]$), they show a lower level of SFA (on average ~4 times lower) than blue-SFG.

2. The intermediate-MXGs show little recent (<1 Gyr) SFA enough to contribute to the total NUV flux, and their MIR luminosity-weighted mean stellar ages (1–5 Gyr) are older than the weak-SFG and younger than the weak-MXG.
3. In the evolution of a galaxy, the weak-SFG could be candidates for the transition stage between blue-SFG and intermediate-MXG, where the star formation is quenched, while the intermediate-MXGs are likely to be placed in an intermediate stage between blue/weak-SFG and weak-MXG, where the morphology is transformed into early types.
4. The transition population is the most abundant at intermediate local densities (outskirts of clusters), suggesting that most of the action takes place at intermediate densities. The relative fraction of weak-SFG versus intermediate-MXG increases as local density decreases. This indicates that the star formation quenching is ongoing at the outskirts, and the process is mostly completed at high density. The morphologies of the intermediate-MXG are mostly early type while the weak-SFGs are late type, meaning that the quenching of star formation occurs earlier than the morphological transformation.
5. The fraction of the weak-SFG to SF galaxies shows a different environmental dependence for different stellar masses. For low-mass galaxies, there are no strong environmental effects. This indicates that SF quenching occurs rapidly in low-mass galaxies, and thus they have already evolved into intermediate-MXG. However, our shallow detection limit at S11 does not allow confirming the intermediate-MXG at low mass ($<10^{10}\ M_{\odot}$), except that intermediate-MXGs are relatively low-mass systems among massive ($>10^{10}\ M_{\odot}$) galaxies and likely to be located in the outer parts of the cluster.

This work is based on observations with *AKARI*, a JAXA project with the participation of ESA. This work was supported by the Korea Science and Engineering Foundation (KOSEF) grant no. 2009-0063616, funded by the Korea government (MEST). J.K. was supported by "KASI–Yonsei Joint Research for the Frontiers of Astronomy and Space Science" program (2011) funded by Korea Astronomy and Space Science Institute. We thank L. Piovan for providing his SED model, and Stephane Charlot and Gustavo Bruzual for kindly sending us the new version of their CB07 model. H.S.H. acknowledges the support of the Centre National d'Etudes Spatiales (CNES). This work is partly based on observations obtained with the MMT, a joint facility operated by the Smithsonian Astrophysical Observatory and the University of Arizona, and with the telescopes at the Kitt Peak National Observatory. This research has made use of the NASA/IPAC Extragalactic Database (NED) which is operated by the Jet Propulsion Laboratory, California Institute of Technology, under contract with the National Aeronautics and Space Administration.

REFERENCES

Abell, G. O. 1958, ApJS, 3, 211
Adami, C., Ilbert, O., Pelló, R., et al. 2008, A&A, 491, 681
Bai, L., Rieke, G. H., Rieke, M. J., Christlein, D., & Zabludoff, A. I. 2009, ApJ, 693, 1840
Baldry, I. K., Balogh, M. L., Bower, R. G., et al. 2006, MNRAS, 373, 469
Balogh, M., Eke, V., Miller, C., et al. 2004, MNRAS, 348, 1355
Bamford, S. P., Nichol, R. C., Baldry, I. K., et al. 2009, MNRAS, 393, 1324
Batuski, D. J., & Burns, J. O. 1985, AJ, 90, 1413
Bekki, K., Couch, W. J., & Shioya, Y. 2002, ApJ, 577, 651
Bell, E. F., McIntosh, D. H., Katz, N., & Weinberg, M. D. 2003, ApJS, 149, 289
Bertin, E., & Arnouts, S. 1996, A&AS, 117, 393
Biviano, A., Metcalfe, L., McBreen, B., et al. 2004, A&A, 425, 33
Blanton, M. R., Eisenstein, D., Hogg, D. W., Schlegel, D. J., & Brinkmann, J. 2005, ApJ, 629, 143
Blanton, M. R., & Moustakas, J. 2009, ARA&A, 47, 159
Boselli, A., Boissier, S., Cortese, L., & Gavazzi, G. 2008, ApJ, 674, 742
Boselli, A., & Gavazzi, G. 2006, PASP, 118, 517
Boselli, A., Lequeux, J., Sauvage, M., et al. 1998, A&A, 335, 53
Bower, R. G., Lucey, J. R., & Ellis, R. S. 1992, MNRAS, 254, 601
Bressan, A., Granato, G. L., & Silva, L. 1998, A&A, 332, 135
Bressan, A., Panuzzo, P., Buson, L., et al. 2006, ApJ, 639, L55
Bruzual, G., & Charlot, S. 2003, MNRAS, 344, 1000
Bundy, K., Ellis, R. S., Conselice, C. J., et al. 2006, ApJ, 651, 120
Bundy, K., Scarlata, C., Carollo, C. M., et al. 2010, ApJ, 719, 1969
Burg, R., Giacconi, R., Huchra, J., et al. 1992, A&A, 259, L9
Butcher, H., & Oemler, A., Jr. 1984, ApJ, 285, 426
Calzetti, D., Armus, L., Bohlin, R. C., et al. 2000, ApJ, 533, 682
Cardelli, J. A., Clayton, G. C., & Mathis, J. S. 1989, ApJ, 345, 245
Chabrier, G. 2003, PASP, 115, 763
Chary, R., & Elbaz, D. 2001, ApJ, 556, 562
Choi, Y., Goto, T., & Yoon, S.-J. 2009a, MNRAS, 395, 637
Choi, Y.-Y., Woo, J.-H., & Park, C. 2009b, ApJ, 699, 1679
Clemens, M. S., Bressan, A., Panuzzo, P., et al. 2009, MNRAS, 392, 982
Cortese, L., & Hughes, T. M. 2009, MNRAS, 400, 1225
Cowie, L. L., Songaila, A., Hu, E. M., & Cohen, J. G. 1996, AJ, 112, 839
Cucciati, O., Iovino, A., Marinoni, C., et al. 2006, A&A, 458, 39
De Propris, R., Colless, M., Peacock, J. A., et al. 2004, MNRAS, 351, 125
Dressler, A. 1980, ApJ, 236, 351
Dressler, A., Oemler, A., Jr., Couch, W. J., et al. 1997, ApJ, 490, 577
Elbaz, D., Daddi, E., Le Borgne, D., et al. 2007, A&A, 468, 33
Fabricant, D., Fata, R., Roll, J., et al. 2005, PASP, 117, 1411
Frogel, J. A., Mould, J., & Blanco, V. M. 1990, ApJ, 352, 96
Gallazzi, A., Bell, E. F., Wolf, C., et al. 2009, ApJ, 690, 1883
Haas, M. R., Schaye, J., & Jeeson-Daniel, A. 2012, MNRAS, 419, 2133
Henry, J. P., Mullis, C. R., Voges, W., et al. 2006, ApJS, 162, 304
Hopkins, P. F., Somerville, R. S., Cox, T. J., et al. 2009, MNRAS, 397, 802
Hwang, H. S., Elbaz, D., Lee, J. C., et al. 2010, A&A, 522, 33
Hwang, H. S., & Park, C. 2009, ApJ, 700, 791
Hwang, N., Lee, M. G., Lee, H. M., et al. 2007, ApJS, 172, 583
Ilbert, O., Capak, P., Salvato, M., et al. 2009, ApJ, 690, 1236
Ilbert, O., Salvato, M., Le Floc'h, E., et al. 2010, ApJ, 709, 644
Im, M., Ko, J., Cho, Y., et al. 2010, J. Korean Astron. Soc., 43, 75
Im, M., Lee, H. M., Lee, M. G., et al. 2008, in ASP Conf. Ser. 399, Panoramic Views of Galaxy Formation and Evolution, ed. T. Kodama, T. Yamada, & K. Aoki (San Francisco, CA: ASP), 382
Jeon, Y., Im, M., Ibrahimov, M., et al. 2010, ApJS, 190, 166
Kaneda, H., Onaka, T., & Sakon, I. 2005, ApJ, 632, L83
Kaneda, H., Onaka, T., Sakon, I., et al. 2008, ApJ, 684, 270
Kauffmann, G., Heckman, T. M., White, S. D. M., et al. 2003, MNRAS, 341, 54
Kauffmann, G., White, S. D. M., Heckman, T. M., et al. 2004, MNRAS, 353, 713
Kennicutt, R. C. 1998, ARA&A, 36, 189
Knapp, G. R., Guhathakurta, P., Kim, D.-W., & Jura, M. A. 1989, ApJS, 70, 329
Knapp, G. R., Gunn, J. E., & Wynn-Williams, C. G. 1992, ApJ, 399, 76
Ko, J., Im, M., Lee, H. M., et al. 2009, ApJ, 695, L198
Kodama, T., & Arimoto, N. 1997, A&A, 320, 41
Koopmann, R. A., & Kenney, J. D. P. 2004, ApJ, 613, 866
Kurtz, M. J., Mink, D. J., Wyatt, W. F., et al. 1992, in ASP Conf. Ser. 25, Astronomical Data Analysis Software and Systems I, ed. D. M. Worrall, C. Biemesderfer, & J. Barnes (San Francisco, CA: ASP), 432
Lee, H. M., Im, M., Wada, T., et al. 2007, PASJ, 59S, 529
Lee, H. M., Kim, S. J., Im, M., et al. 2009a, PASJ, 61, 375
Lee, J. H., Hwang, H. S., Lee, M. G., Lee, J. C., & Matsuhara, H. 2010, ApJ, 719, 1946
Lee, J. H., Lee, M. G., Park, C., & Choi, Y.-Y. 2008, MNRAS, 389, 1791
Lee, M. G., Lee, H. M., Im, M., et al. 2009b, in ASP Conf. Ser. 418, AKARI, a Light to Illuminate the Misty Universe, ed. T. Onaka, G. J. White, T. Nakagawa, & I. Yamamura (San Francisco, CA: ASP), 241
Lewis, I., Balogh, M., De Propris, R., et al. 2002, MNRAS, 334, 673
Li, I. H., Glazebrook, K., Gilbank, D., et al. 2011, MNRAS, 411, 1869
Lin, C. C., & Shu, F. H. 1964, ApJ, 140, 646
Lintott, C. J., Schawinski, K., Slosar, A., et al. 2008, MNRAS, 389, 1179
Maraston, C. 2005, MNRAS, 362, 799
Marigo, P., & Girardi, L. 2007, A&A, 469, 239
Masters, K. L., Mosleh, M., Romer, A. K., et al. 2010, MNRAS, 405, 783
Matsuhara, H., Wada, T., Matsuura, S., et al. 2006, PASJ, 58, 673

Mullis, C. R., Henry, J. P., Gioia, I. M., et al. 2001, ApJ, 553, L115
Murakami, H., Baba, H., Barthel, P., et al. 2007, PASJ, 59, S369
Obrić, M., Ivezić, Ž., Best, P. N., et al. 2006, MNRAS, 370, 1677
Panuzzo, P., Rampazzo, R., Bressan, A., et al. 2011, A&A, 528, 10
Park, C., & Hwang, H. S. 2009, ApJ, 699, 1595
Peng, Y., Lilly, S. J., Kovač, K., et al. 2010, ApJ, 721, 193
Pimbblet, K. A., Smail, I., Kodama, T., et al. 2002, MNRAS, 331, 333
Piovan, L., Tantalo, R., & Chiosi, C. 2003, A&A, 408, 559
Poggianti, B. M., Bridges, T. J., Carter, D., et al. 2001, ApJ, 563, 118
Polletta, M., Tajer, M., Maraschi, L., et al. 2007, ApJ, 663, 81
Postman, M., Franx, M., Cross, N. J. G., et al. 2005, ApJ, 623, 721
Salim, S., & Rich, R. M. 2010, ApJ, 714, L290
Salpeter, E. E. 1955, ApJ, 121, 161
Sánchez, S. F., Cardiel, N., Verheijen, M. A. W., Pedraz, S., & Covone, G. 2007, MNRAS, 376, 125
Sánchez-Blázquez, P., Jablonka, P., Noll, S., et al. 2009, A&A, 499, 47
Schlegel, D. J., Finkbeiner, D. P., & Davis, M. 1998, ApJ, 500, 525
Shim, H., Im, M., Lee, H. M., et al. 2011, ApJ, 727, 14
Silva, L., Granato, G. L., Bressan, A., & Danese, L. 1998, ApJ, 509, 103
Sobral, D., Best, P. N., Smail, I., et al. 2011, MNRAS, 411, 675
Spinoglio, L., Malkan, M. A., Rush, B., Carrasco, L., & Recillas-Cruz, E. 1995, ApJ, 453, 616
Temi, P., Mathews, W. G., & Brighenti, F. 2005, ApJ, 622, 235
Trager, S. C., Faber, S. M., Worthey, G., & González, J. J. 2000, AJ, 120, 165
Tran, K.-V. H., Saintonge, A., Moustakas, J., et al. 2009, ApJ, 705, 809
Valdes, F. 1995, Guide to the HYDRA Reduction Task DOHYDRA, available at http://iraf.net/irafdocs/dohydra.pdf
van den Bergh, S. 1976, ApJ, 206, 883
van Dokkum, P. G. 2001, PASP, 113, 1420
Vega, O., Bressan, A., Panuzzo, P., et al. 2010, ApJ, 721, 1090
Weinmann, S. M., van den Bosch, F. C., Yang, X., & Mo, H. J. 2006, MNRAS, 366, 2
Willmer, C. N. A., Faber, S. M., Koo, D. C., et al. 2006, ApJ, 647, 853
Wolf, C., Aragón-Salamanca, A., Balogh, M., et al. 2009, MNRAS, 393, 1302
Xilouris, E. M., Madden, S. C., Galliano, F., Vigroux, L., & Sauvage, M. 2004, A&A, 416, 41
Yi, S. K., Yoon, S.-J., Kaviraj, S., et al. 2005, ApJ, 619, L111
York, D. G., Adelman, J., Anderson, J. E., Jr., et al. 2000, AJ, 120, 1579